Orbital diamagnetism of graphene nanostructures

Master Thesis

Orbital diamagnetism of graphene nanostructures
（グラフェンナノ構造体における軌道反磁性）

Yuya Ominato

Department of Physics, Graduate School of Science
Tohoku University

2012

Contents

Chapter 1

Introduction

Graphene is one-atom-thick crystal which consists of a single sheet of carbon atoms, and the thinnest crystal ever produced. Theoretically, the electronic property of graphene was first studied as a simplified model of three-dimensional graphite, which is a layered material composed of graphenes. [1, 2, 3, 4] Two-dimensional graphene itself was considered as a purely theoretical material, but after the fabrication of graphene using a mechanical exfoliation,[5] enormous effort has been devoted to understanding its physical properties experimentally and theoretically. [6] Graphene has a characteristic band structure, where the valence and conduction bands stick together with a linear dispersion at corners of Brillouin zone represented as K and K′. Using an effective-mass approximation, the electronic states of graphene in the vicinity of Fermi level are described by the relativistic Dirac equation with vanishing rest mass. [1, 2, 3, 7, 8, 9, 10] This notable electronic band structure

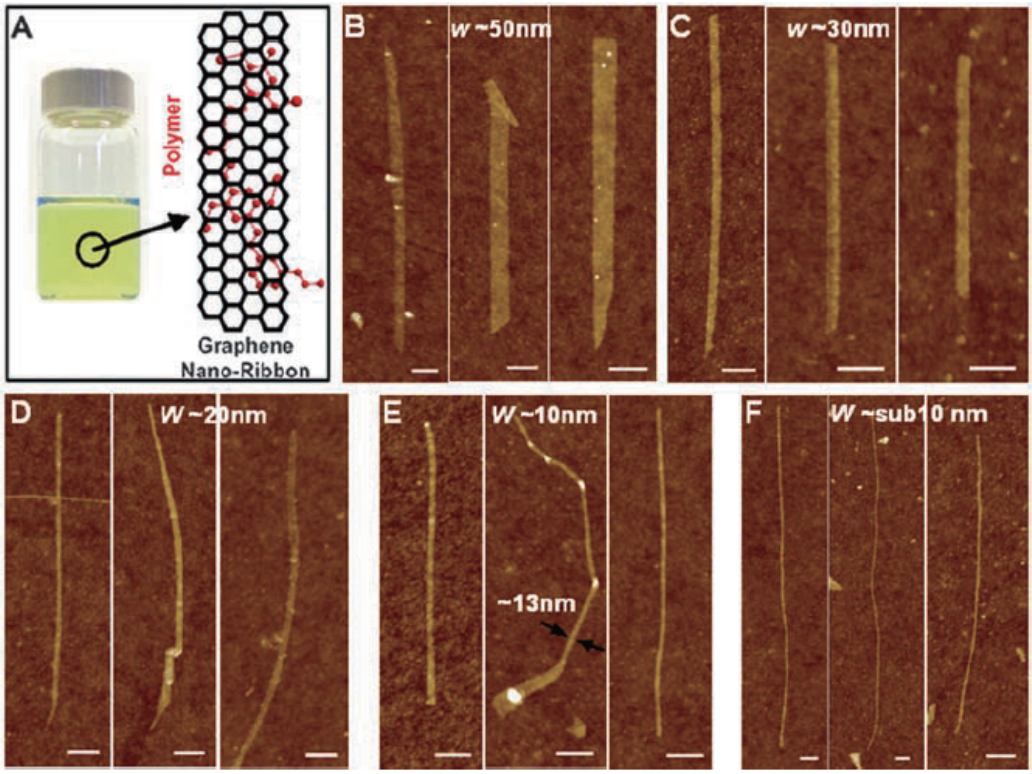

Figure 1.1: Chemically derived graphene nanoribbons with several width. All scale bars indicate 100nm. From [19].

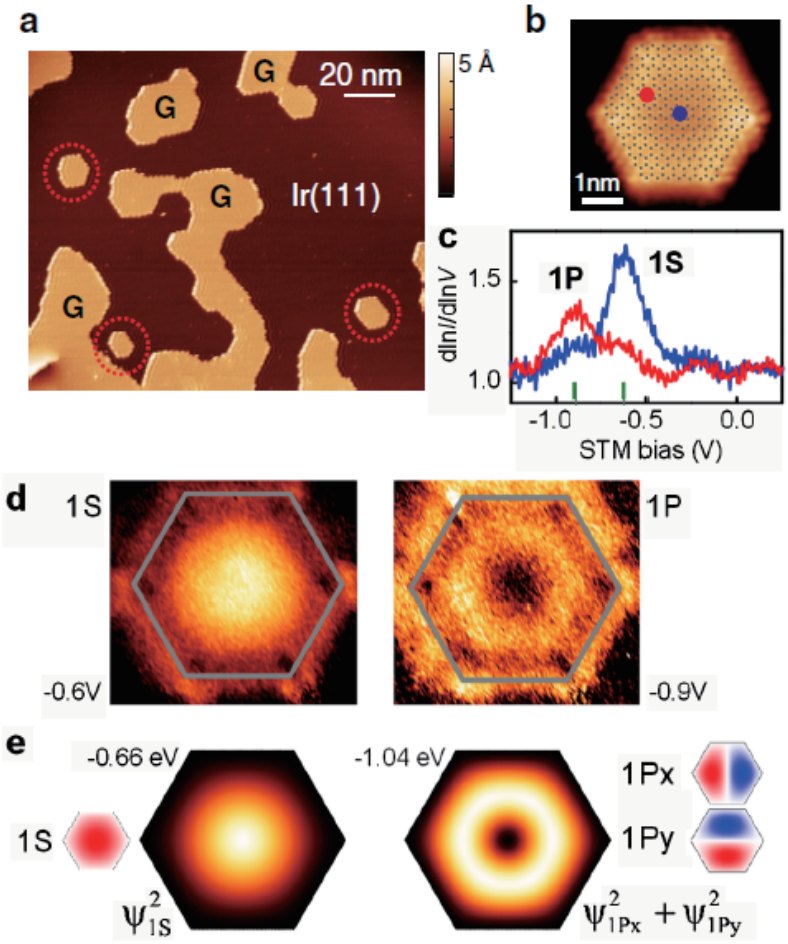

Figure 1.2: STM imaging and spectroscopy on graphene flakes grown by CVD on Ir(111). (a) Large-scale STM image of graphene flakes (G) on an Ir(111) subtrate. Small graphene flakes have been indicated by red circles. (b) STM topography of a small graphene flake with an overlaid atomic model which has perfect hexagonal symmetry with 7 benzene ring along edges. (c) $d\ln I/d\ln V_b$ spectra measured on the points indicated in (b), the green bars indicate the bias voltages corresponding to the two resonances in the spectra shown in (c). (e) The corresponding LDOS maps calculated for a particle in a box at the indicated energies and the underlying eigenstates. From [22].

gives rise to various unusual physical properties different from the conventional electron systems. [10, 11, 12, 13, 14, 15, 16]

Recently, developments in experimental techniques enables to fabricate a various kind of nanostructures such as ribbons and flakes out of graphene. Graphene nanoribbons were first fabricated by top-down approaches using lithographic technique for exfoliated graphene films. [17, 18] Later, with the emergence of bottom-up approaches such as chemical synthesis and chemical vapor deposition (CVD), the control of the final system geometry has been significantly improved, and it is now possible to produce graphene systems of different size and forms with atomically smooth edges, ranging from the quasi-one dimensional ribbons to the zero-dimensional flakes. [19, 20, 21, 22, 23, 24] Figures 1.1 and 1.2 show chemically derived graphene nanoribbons, and CVD-grown graphene flakes, respectively. Alternatively, the graphene ribbons with atomically smooth edges can be fabricated by unzipping carbon nanotubes with chemical oxidative process, as shown in Fig. 1.3. [20, 21]

Electronic structures of graphene nanostructures strongly depend on the shapes and the edge configurations. Theoretically, two different edge forms, armchair and zigzag, have been considered as representative forms of interface as shown in Fig. 1.4. It was shown that the zigzag edge is accompanied by zero-energy edge state localized at the boundary, [25] and it is experimentally observed using scanning tunneling spectroscopy (Fig. 1.5). [26] So far, a number of theoretical researches have been devoted to understanding the electronic properties in the graphene ribbon [25, 27, 28, 29, 30, 31, 32, 33, 34] and graphene nanoflakes. [35, 36, 37, 38, 39, 40, 41, 42, 43, 44]

In this thesis, we study the orbital diamagnetism of graphene nanostructures. Generally, the orbital magnetism sensitively depends on the electronic band structure of the system, and sometimes largely deviates from the conventional Landau diamagnetism of free electrons. Particularly, the diamagentism tends to be large in narrow gap systems such as graphite [3, 45, 46] and bismuth [47, 48] due to small effective mass, and becomes even greater in graphene which is a truly zero-gap system. The magnetic susceptibility of bulk graphene contains a singularity expressed as a δ function in Fermi energy ε_{F}, which diverges at Dirac point ($\varepsilon_{\mathrm{F}} = 0$) where the two bands stick. [3, 49, 50, 51, 52, 53, 54, 55, 56, 57, 58, 59] The singular magentic behavior is expected to be significantly modified in graphene nanostructures due to the quantum confinement effect. The orbital magnetism of finite-sized graphene system was theoretically studied for carbon nanotubes [60, 61, 62] and graphene ribbons [28, 63] while the dependence on the system size and atomic configuraions, nor the

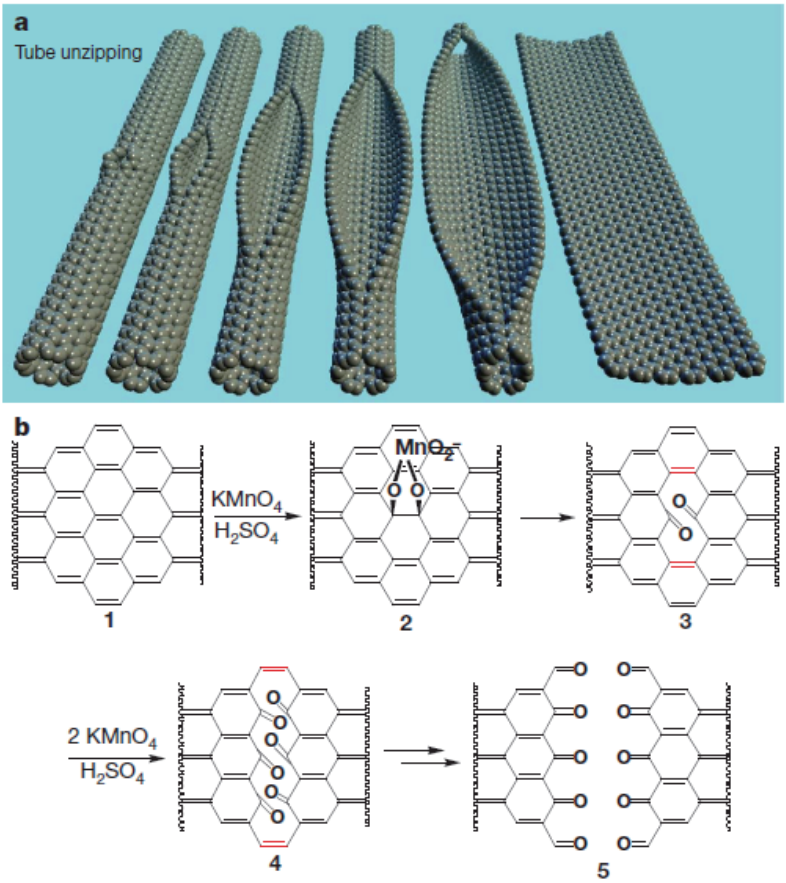

Figure 1.3: (a) Representation of the gradual unzipping of one wall of a carbon nanotube to form a nanoribbon. Oxygenated sites are not shown. (b) The proposed chemical mechanism of nanotube unzipping. From [20].

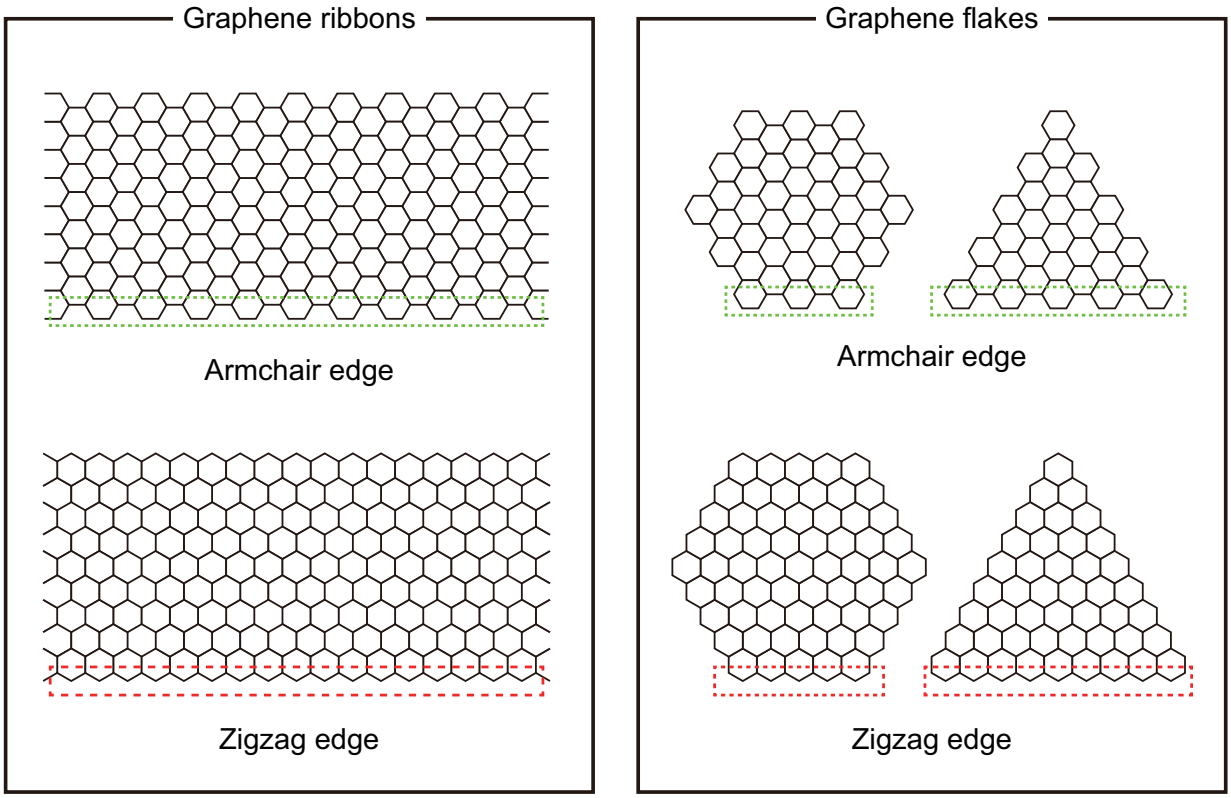

Figure 1.4: Geometry of graphene nanostructures.

relation to the bulk limit are not well understood.

Experimentally, the magnetic property of graphene-based materials was investigated for bulk graphite [64, 65, 66], nanographite [67], and exfoliated graphene nanocrystals [68]. There the susceptibility always contains strong diamagnetic background due to the orbital effect, whereas it is also contributed by the spin paramagnetism, [68] and the spin magentic ordering [65, 66, 67, 69] which may be caused by the zero-energy edge states, [28, 43, 44] and atomic defects. In any case, correct understanding of the orbital susceptibility of finite graphene systems is important to describe the overall magentic property in realistic graphene systems.

In this thesis, we investigate the orbital diamagnetism of graphene ribbons and flakes with various sizes, shapes and edge configurations. For each case we calculate the orbital magnetic susceptibility and the diamagnetic electric current distribution, to find characteristic properties peculiar to each different case, and also general tendencies independent of the configuration. For the theoretical model, we use the tight-binding model or the continuum Dirac model depending on the problem. The latter is derived from the tight-binding model using the effective mass approximation, and gives the equivalent result to the original as long as the system size is much larger than the lattice spacing. The virtue of the continuum approach is to enable one to treat the problem analyitically and also to extract the scale-invariant properties originating purely from the nature of the massless Dirac Hamiltonian. We apply the continuum Dirac model to the graphene ribbons, while use the original tight-binding model for graphene flakes where the continuum approach becomes overcomplicated.

The thesis is organized as follows: In Chapter. 2, we introduce the tight-binding model and the effective Dirac model to describe in graphene electrons. In Chapter. 3 and 4, we discuss the orbital diamagnetism of graphene ribbons and graphene flakes, respectively.

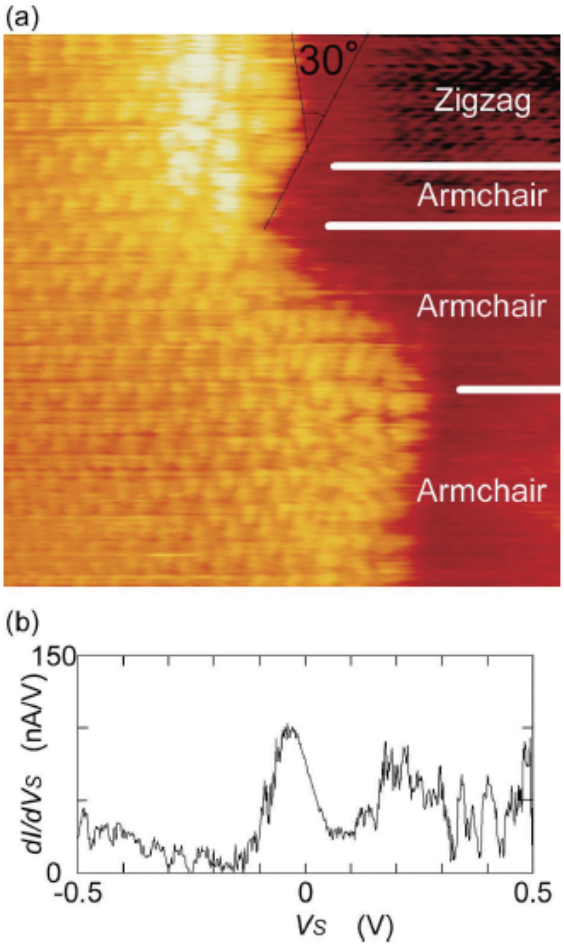

Figure 1.5: (a) An atomically resolved UHV STM image of zigzag and armchair edges ($9\times9\text{nm}^2$). (b) Typical dI/dV_S curve from STS data at a zigzag edge. From [26].

The conclusion and summary is given in Chapter. 5.

Chapter 2

Band model of graphene

In this chaper, we review the band model to describe electrons in graphene which will be used in the following chapters. We first introduce the tight-binding model, and then derive the continuum Dirac model based on it by applying the effective mass approximation. In the last section, we calculate the orbital magnetic susceptibility of bulk graphene using the effective Dirac model, which is shown to be a δ function in the Fermi energy.

2.1 Atomic structure

The Lattice structure of graphene and the first Brillouin zone are shown in Fig. 2.1. We have the primitive translation vectors

$$\boldsymbol{a} = a(1, 0),\ \boldsymbol{b} = a(-1/2, \sqrt{3}/2), \tag{2.1}$$

and the vectors connecting nearest neighbor carbon atoms

$$\boldsymbol{\tau}_1 = a(0, 1/\sqrt{3}),\ \boldsymbol{\tau}_2 = a(-1/2, -1/2\sqrt{3}),\ \boldsymbol{\tau}_1 = a(1/2, -1/2\sqrt{3}), \tag{2.2}$$

where a is the lattice constant given by $a \approx 0.246$nm. A hexagonal unit cell contains two carbon atoms, which will be denoted by A (black) and B (white). Afterward, we consider boundary conditions for graphene ribbons, so that we define η as the angle between the x and x' axes, which is $\pi/6$ for the zigzag and 0 for the armchair boundary.

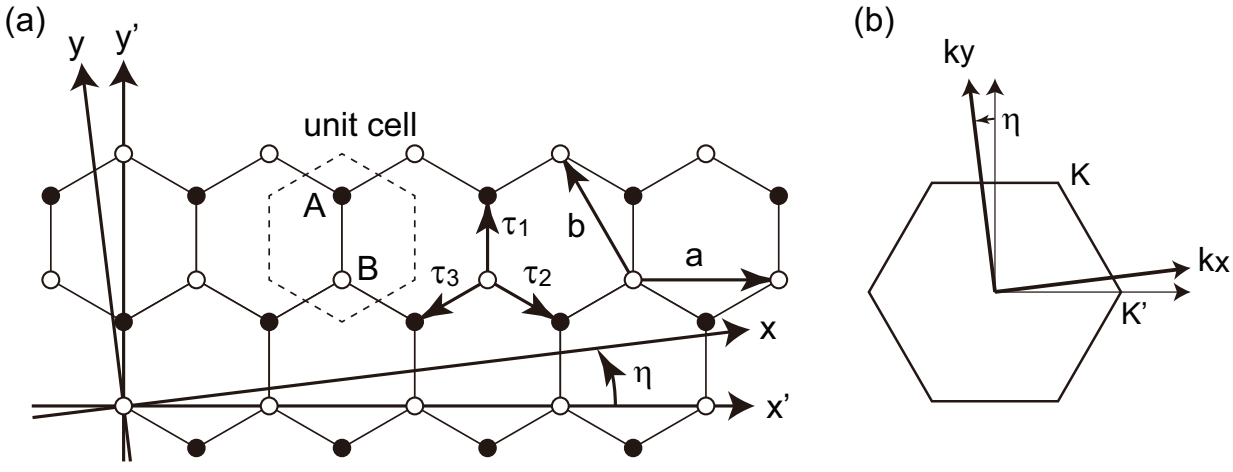

Figure 2.1: (a) Lattice structures and (b) first Brillouin zone of graphene.

The primitive reciprocal lattice vectors $\boldsymbol{a}^*$ and $\boldsymbol{b}^*$ are given by

$$\boldsymbol{a}^* = 2\pi/a(1, 1/\sqrt{3}),\ \boldsymbol{b}^* = 2\pi/a(0, 2/\sqrt{3}). \tag{2.3}$$

The K and K$'$ points at the corners of the Brillouin zone are given as

$$\boldsymbol{K} = 2\pi/a(1/3, 1/\sqrt{3}),\ \boldsymbol{K}' = 2\pi/a(2/3, 0), \tag{2.4}$$

respectively. We have the relations between $\boldsymbol{\tau}_1, \boldsymbol{\tau}_2, \boldsymbol{\tau}_3$ and $\boldsymbol{K}, \boldsymbol{K}'$

$$\exp(i\boldsymbol{K}\cdot\boldsymbol{\tau}_1) = \omega,\ \exp(i\boldsymbol{K}\cdot\boldsymbol{\tau}_2) = \omega^{-1},\ \exp(i\boldsymbol{K}\cdot\boldsymbol{\tau}_3) = 1, \tag{2.5}$$

$$\exp(i\boldsymbol{K}'\cdot\boldsymbol{\tau}_1) = 1,\ \exp(i\boldsymbol{K}'\cdot\boldsymbol{\tau}_2) = \omega^{-1},\ \exp(i\boldsymbol{K}'\cdot\boldsymbol{\tau}_3) = \omega, \tag{2.6}$$

where $\omega = \exp(2\pi i/3)$.

2.2 Tight-binding model

The motion of graphene electrons can be modelled by the nearest-neighbor tight-binding model of p_z orbitals. In a tight-binding model, the wave function is written as

$$\psi(\boldsymbol{r}) = \sum_{\boldsymbol{R}_\mathrm{A}} \psi_\mathrm{A}(\boldsymbol{R}_\mathrm{A})\phi(\boldsymbol{r}-\boldsymbol{R}_\mathrm{A}) + \sum_{\boldsymbol{R}_\mathrm{B}} \psi_\mathrm{B}(\boldsymbol{R}_\mathrm{B})\phi(\boldsymbol{r}-\boldsymbol{R}_\mathrm{B}), \tag{2.7}$$

where $\boldsymbol{R}_\mathrm{A} = n_a\boldsymbol{a} + n_b\boldsymbol{b} + \boldsymbol{\tau}_1$ and $\boldsymbol{R}_\mathrm{B} = n_a\boldsymbol{a} + n_b\boldsymbol{b}$, with integer n_a and n_b, are the positions of A-sites and B-sites, respectively, and $\phi(\boldsymbol{r})$ denotes the wave function of the p_z orbital of a carbon atom located at the origin. Let $-\gamma_0$ be the transfer integral between nearest-neighbor carbon atoms and choose the energy origin at that of the carbon p_z level. The parameter γ_0 was experimentally estimated in the bulk graphite as $\gamma_0 \approx 3$eV.[70, 71] We substitute this wave function into the Schrödinger equation

$$H\psi(\boldsymbol{r}) = \varepsilon\psi(\boldsymbol{r}), \tag{2.8}$$

multiply it by $\psi(\boldsymbol{r}-\boldsymbol{R}_j),\ (j = \mathrm{A}, \mathrm{B})$, and then integrate it in all space. Then we have

$$\begin{aligned}
\varepsilon\psi_\mathrm{A}(\boldsymbol{R}_\mathrm{A}) &= -\gamma_0 \sum_{l=1}^{3} \psi_\mathrm{B}(\boldsymbol{R}_\mathrm{A} - \boldsymbol{\tau}_l), \\
\varepsilon\psi_\mathrm{B}(\boldsymbol{R}_\mathrm{B}) &= -\gamma_0 \sum_{l=1}^{3} \psi_\mathrm{A}(\boldsymbol{R}_\mathrm{B} + \boldsymbol{\tau}_l),
\end{aligned} \tag{2.9}$$

where the overlap integral between nearest A and B sites is completely neglected for simplicity.

Using Bloch's theorem, we have

$$\psi_\mathrm{A}(\boldsymbol{R}_\mathrm{A}) \propto f_\mathrm{A}(\boldsymbol{k})\exp(i\boldsymbol{k}\cdot\boldsymbol{R}_\mathrm{A}), \tag{2.10}$$

$$\psi_\mathrm{B}(\boldsymbol{R}_\mathrm{B}) \propto f_\mathrm{B}(\boldsymbol{k})\exp(i\boldsymbol{k}\cdot\boldsymbol{R}_\mathrm{B}), \tag{2.11}$$

and we derive

$$\begin{pmatrix} 0 & h_\mathrm{AB}(\boldsymbol{k}) \\ h_\mathrm{AB}(\boldsymbol{k})^* & 0 \end{pmatrix} \begin{pmatrix} f_\mathrm{A}(\boldsymbol{k}) \\ f_\mathrm{B}(\boldsymbol{k}) \end{pmatrix} = \varepsilon \begin{pmatrix} f_\mathrm{A}(\boldsymbol{k}) \\ f_\mathrm{B}(\boldsymbol{k}) \end{pmatrix}, \tag{2.12}$$

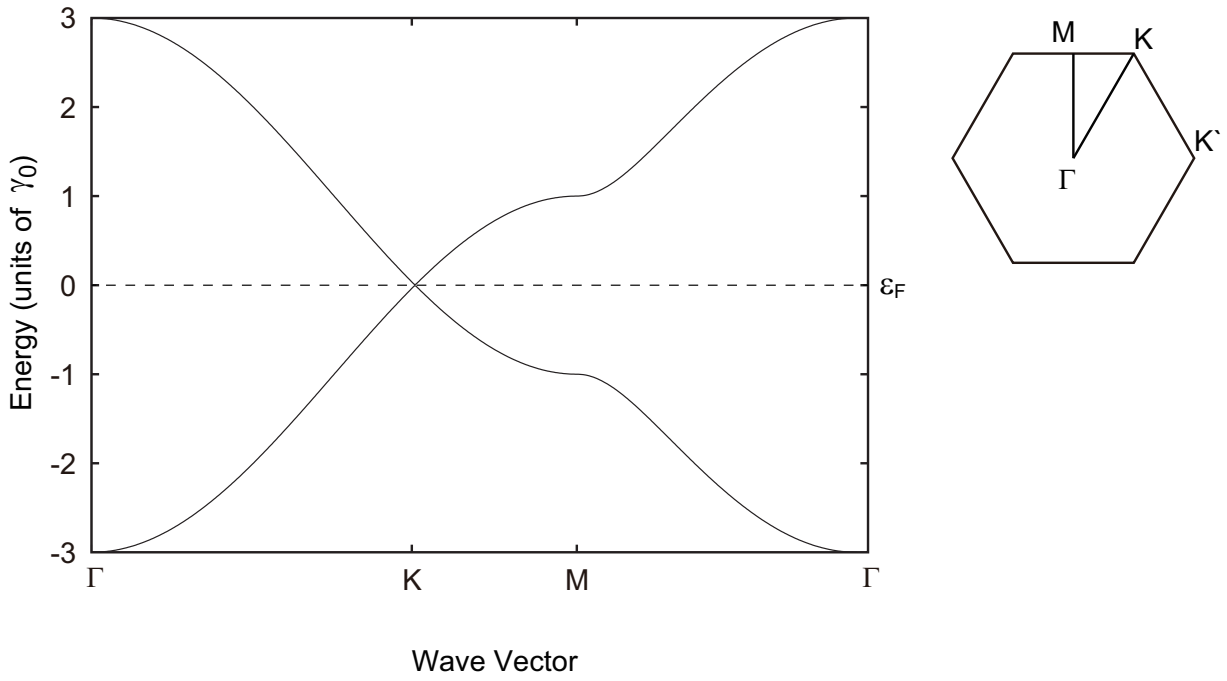

Figure 2.2: The band structure of graphene obtained in the nearest-neighbor tight-binding model along $\Gamma \to \mathrm{K} \to \mathrm{M} \to \Gamma$. The Fermi level lies at the center $\varepsilon = 0$.

with

$$h_{\mathrm{AB}}(\boldsymbol{k}) = -\gamma_0 \sum_{l=1}^{3} \exp(-i\boldsymbol{k}\cdot\boldsymbol{\tau}_l). \tag{2.13}$$

The energy bands are given by

$$\varepsilon_{\pm}(\boldsymbol{k}) = \pm|h_{\mathrm{AB}}(\boldsymbol{k})|. \tag{2.14}$$

The band structure is shown in Fig. 2.2. Using eq. (2.5) and (2.6), it is clear that $\varepsilon_{\pm}(\boldsymbol{K}) = \varepsilon_{\pm}(\boldsymbol{K}') = 0$, so that the valence and conduction bands stick together at K and K′ points. Near the K and K′ points, we have

$$\varepsilon_{\pm}(\boldsymbol{K}+\boldsymbol{k}) = \varepsilon_{\pm}(\boldsymbol{K}'+\boldsymbol{k}) = \pm\hbar v\sqrt{k_x^2+k_y^2}, \tag{2.15}$$

with

$$\hbar v = \frac{\sqrt{3}a\gamma_0}{2}, \tag{2.16}$$

for $|\boldsymbol{k}|a \ll 1$.

2.3 Effective-mass description

In the following, we shall derive an effective-mass ($\boldsymbol{k}\cdot\boldsymbol{p}$) equation describing states in the vicinity of K and K′ points based on the nearest-neighbor tight-binding model. We consider the coordinates (x, y) rotated around the origin by η as well as original (x', y') as shown in Fig. 2.1.

For a state in the vicinity of zero energy, the wave function can be written as a linear combination of the band states in the vicinity of K and K′ points. There, a small deviation from exact K (K′) point can be included as a slowly-varying envelope function multiplied by Bloch factor $e^{i\boldsymbol{K}\cdot\boldsymbol{r}}$ ($e^{i\boldsymbol{K}'\cdot\boldsymbol{r}}$). As a result, the wavefuncion is written as

$$\begin{aligned}\psi_{\mathrm{A}}(\boldsymbol{R}_{\mathrm{A}}) &= e^{i\boldsymbol{K}\cdot\boldsymbol{R}_{\mathrm{A}}}F_{\mathrm{A}}^{\mathrm{K}}(\boldsymbol{R}_{\mathrm{A}}) + e^{i\eta}e^{i\boldsymbol{K}'\cdot\boldsymbol{R}_{\mathrm{A}}}F_{\mathrm{A}}^{\mathrm{K}'}(\boldsymbol{R}_{\mathrm{A}}),\\ \psi_{\mathrm{B}}(\boldsymbol{R}_{\mathrm{B}}) &= -\omega e^{i\eta}e^{i\boldsymbol{K}\cdot\boldsymbol{R}_{\mathrm{B}}}F_{\mathrm{B}}^{\mathrm{K}}(\boldsymbol{R}_{\mathrm{B}}) + e^{i\boldsymbol{K}'\cdot\boldsymbol{R}_{\mathrm{B}}}F_{\mathrm{B}}^{\mathrm{K}'}(\boldsymbol{R}_{\mathrm{B}}),\end{aligned} \tag{2.17}$$

in terms of the slowly-varying envelope functions $F_{\mathrm{A}}^{\mathrm{K}}, F_{\mathrm{B}}^{\mathrm{K}}, F_{\mathrm{A}}^{\mathrm{K}'}$, and $F_{\mathrm{B}}^{\mathrm{K}'}$. The phase factors $e^{i\eta}$ and $-\omega e^{i\eta}$ are attached to simplify the final equation. We substitute Eq. (2.17) for ψ's in Eq. (2.9), and derive the differential equations for the envelop function F, using the property that it is slowly varying in the atomic scale. We end up with the Schrödinger equation for the envelop functions, [2, 3, 7, 8, 9, 10]

$$\mathcal{H}_0\boldsymbol{F}(\boldsymbol{r}) = \varepsilon\boldsymbol{F}(\boldsymbol{r}), \tag{2.18}$$

with

$$\mathcal{H}_0 = \hbar v\begin{pmatrix} 0 & \hat{k}_x - i\hat{k}_y & 0 & 0\\ \hat{k}_x + i\hat{k}_y & 0 & 0 & 0\\ 0 & 0 & 0 & \hat{k}_x + i\hat{k}_y\\ 0 & 0 & \hat{k}_x - i\hat{k}_y & 0\end{pmatrix}, \tag{2.19}$$

where $\hat{\boldsymbol{k}} = -i\nabla$, and

$$\boldsymbol{F}(\boldsymbol{r}) = \begin{pmatrix} F_{\mathrm{A}}^{\mathrm{K}}(\boldsymbol{r})\\ F_{\mathrm{B}}^{\mathrm{K}}(\boldsymbol{r})\\ F_{\mathrm{A}}^{\mathrm{K}'}(\boldsymbol{r})\\ F_{\mathrm{B}}^{\mathrm{K}'}(\boldsymbol{r})\end{pmatrix}. \tag{2.20}$$

This is relativistic Dirac equation with vanishing rest mass known as Weyl's equation for a neutrino.

2.4 Orbital diamagnetism of bulk graphene

We derive the orbital magnetic susceptibility for bulk graphene using the Dirac model. In a magnetic field B perpendicular to the graphene, Hamiltonian for the K point is written as

$$\mathcal{H} = \hbar\omega_{\mathrm{B}}\begin{pmatrix} 0 & a\\ a^\dagger & 0\end{pmatrix}, \tag{2.21}$$

where $a = (\ell_{\mathrm{B}}/\sqrt{2})(\hat{k}_x - i\hat{k}_y)$, $\hbar\omega_{\mathrm{B}} = \sqrt{2}\hbar v/\ell_{\mathrm{B}}$, $\ell_{\mathrm{B}} = \sqrt{c\hbar/(eB)}$, $\hat{\boldsymbol{k}} = -i\boldsymbol{\nabla} + (e/c\hbar)\boldsymbol{A}$, and $\boldsymbol{A}(\boldsymbol{r})$ is the vector potential giving the magnetic field by $\boldsymbol{B} = \nabla\times\boldsymbol{A}$. We have $[a, a^\dagger] = 1$. We shall define a function $h_n(x, y)$ such that

$$h_n(x, y) = \frac{(a^\dagger)^n}{\sqrt{n}}h_0(x, y), \tag{2.22}$$

with

$$ah_0(x, y) = 0. \tag{2.23}$$

Then, we have

$$a^\dagger h_n = \sqrt{n+1}h_{n+1}, \tag{2.24}$$

$$a h_{n+1} = \sqrt{n+1}h_n, \tag{2.25}$$

$$a^\dagger a h_n = n h_n. \tag{2.26}$$

The energy of n-th Landau level is then given by

$$\varepsilon_n = \mathrm{sgn}(n)\hbar\omega_\mathrm{B}\sqrt{|n|}, \tag{2.27}$$

and the wave function by

$$\boldsymbol{F}_n^\mathrm{K} = \begin{pmatrix} \mathrm{sgn}(n)h_{|n|-1} \\ h_{|n|} \end{pmatrix}, \tag{2.28}$$

where $n = 0, \pm1, \pm2, \cdots$ and $\mathrm{sgn}(n)$ is $n/|n|$ for $n \neq 0$, and 0 for $n = 0$. Each Landau level has degeneracy $g = 1/(2\pi\ell_\mathrm{B})$ per unit area. Similar expressions can be derived for the K′ point.

The magnetization M is given by the derivative of thermodynamic function Ω

$$M = -\left(\frac{\partial\Omega}{\partial B}\right)_{\mu,T}, \tag{2.29}$$

where μ is the chemical potential and T is the temperature. Since the magnetization is written as $M = \chi B$ in a weak magnetic field, the susceptibility χ is obtained by calculating Ω up to the order of B^2, and using

$$\Delta\Omega = -\frac{1}{2}\chi B^2. \tag{2.30}$$

For graphene, the thermodynamic function is given by

$$\begin{aligned}\Omega &= -k_\mathrm{B}T g_\mathrm{v} g_\mathrm{s} g \sum_{n=-\infty}^{\infty} C(|\varepsilon_n|)\ln\{1+\exp[(\mu-\varepsilon_n)/k_\mathrm{B}T]\}, \\ &= -k_\mathrm{B}T g_\mathrm{v} g_\mathrm{s} g \sum_{n=0}^{\infty} C(\hbar\omega_\mathrm{B}\sqrt{n})\left(1-\frac{1}{2}\delta_{n0}\right) \\ &\qquad \times \ln[1+2\exp(\mu/k_\mathrm{B}T)\cosh(\hbar\omega_\mathrm{B}\sqrt{n}/k_\mathrm{B}T)+\exp(2\mu/k_\mathrm{B}T)],\end{aligned} \tag{2.31}$$

where $g_\mathrm{v} = g_\mathrm{s} = 2$ are the valley and spin degeneracies, respectively, and $C(\varepsilon)$ is a cutoff function given by

$$C(\varepsilon) = \frac{\varepsilon_\mathrm{c}^\alpha}{\varepsilon^\alpha + \varepsilon_\mathrm{c}^\alpha}, \tag{2.32}$$

with cutoff energy ε_c and parameter α, ($\alpha > 2$). Consider a smooth function $F(x)$ and its integral

$$\int_0^\infty F(x)\mathrm{d}x = \int_0^{h/2} F(x)\mathrm{d}x + \sum_{j=1}^{\infty}\int_{-h/2}^{h/2} F(x+hj)\mathrm{d}x, \tag{2.33}$$

where h is a small positive number. For sufficiently small h, we have

$$h\left[\frac{1}{2}F(0)+\sum_{j=1}^{\infty}F(hj)\right] = \int_0^\infty F(x)\mathrm{d}x - \frac{1}{12}h^2\left[F'(0)+\frac{1}{2}F'(\infty)\right]+\cdots. \tag{2.34}$$

Let $h = (\hbar\omega_{\rm B})^2$, $x = nh$, and

$$F(x) = C(\sqrt{x}) \ln[1 + 2\exp(\mu/k_{\rm B}T)\cosh(\sqrt{x}/k_{\rm B}T) + \exp(2\mu/k_{\rm B}T)]. \tag{2.35}$$

Then, we have

$$\begin{aligned}
\Omega =& -\frac{k_{\rm B}T g_{\rm v} g_{\rm s}}{2\pi\ell_{\rm B}^2(\hbar\omega_{\rm B})^2} h \sum_{n=0}^{\infty} C(\sqrt{x}) \left(1 - \frac{1}{2}\delta_{n0}\right) \\
&\times \ln[1 + 2\exp(\mu/k_{\rm B}T)\cosh(\sqrt{nh}/k_{\rm B}T) + \exp(2\mu/k_{\rm B}T)], \\
=& -\frac{k_{\rm B}T g_{\rm v} g_{\rm s}}{2\pi\ell_{\rm B}^2(\hbar\omega_{\rm B})^2} \int_0^{\infty} C(\sqrt{x}) \ln[1 + 2\exp(\mu/k_{\rm B}T)\cosh(\sqrt{nh}/k_{\rm B}T) + \exp(2\mu/k_{\rm B}T)]{\rm d}x \\
&+ \frac{k_{\rm B}T g_{\rm v} g_{\rm s}}{2\pi\ell_{\rm B}^2(\hbar\omega_{\rm B})^2} \frac{h^2}{12} \frac{\exp(\mu/k_{\rm B}T)/(k_{\rm B}T)^2}{[1 + \exp(\mu/k_{\rm B}T)]^2} + \cdots .
\end{aligned} \tag{2.36}$$

Note that the derivative of the cutoff function at $x = 0$ can safely be neglected. Therefore, we have

$$\Delta\Omega = g_{\rm v} g_{\rm s} \frac{e^2 v^2}{12\pi c^2} B^2 \int_{-\infty}^{\infty} \left(-\frac{\partial f(\varepsilon)}{\partial\varepsilon}\right) \delta(\varepsilon){\rm d}\varepsilon, \tag{2.37}$$

where $f(\varepsilon) = 1/[1 + e^{\beta(\varepsilon-\mu)}]$ is the Fermi distribution function with the chemical potential μ. The susceptibility is derived as [3, 49, 50]

$$\begin{aligned}
\chi_{\rm Dirac}(\mu; T) &= -g_{\rm v} g_{\rm s} \frac{e^2 v^2}{6\pi c^2} \int_{-\infty}^{\infty} \left(-\frac{\partial f(\varepsilon)}{\partial\varepsilon}\right) \delta(\varepsilon){\rm d}\varepsilon. \\
&= -g_v g_s \frac{e^2 v^2}{24\pi c^2} \frac{1}{k_B T \cosh^2[\mu/(2k_B T)]}.
\end{aligned} \tag{2.38}$$

In the limit of $T \to 0$, the susceptibility becomes

$$\chi_{\rm Dirac}(\mu) = -g_{\rm v} g_{\rm s} \frac{e^2 v^2}{6\pi c^2} \delta(\mu). \tag{2.39}$$

Note that this expression is independent of the detail of the cutoff function. Eq. (2.39) indicates that the susceptibility diverges at the Dirac point and vanishes otherwise. This is significantly different from the conventional Landau diamagnetism, in which the susceptibility is simply proportional to the density of states. The calculation of the Landau diamagnetism is briefly presented in Appendix A.

Chapter 3

Graphene Ribbons

3.1 Formulations

3.1.1 Effective-mass description

In this chapter, we condiser the zigzag and armchair graphene ribbons, of which atomic structures are illustrated in Fig. 3.1 (a) and (b), respectively. For both cases we set y-axis along the ribbon, and set $x = 0$ and L_x to the line of missing sites nearest from the edge. η is the angle between x axis and $\boldsymbol{a}$, which is $\pi/6$ for zigzag, and 0 for armchair boundary.

The electronic states of the graphene ribbon can be correctly described by setting the appropriate boundary condition to the effective-mass Hamiltonian. [31] Now the eigenstates are labeled by k_y since the system is translationally symmetric along y-axis. An eigenstate of Eq. (2.18) with k_y and the energy ε is generally written as

$$\boldsymbol{F}(\boldsymbol{r}) = e^{ik_y y} \begin{pmatrix} Ae^{ik_x x} + Be^{-ik_x x} \\ s\left(Ae^{i(k_x x+\theta)} - Be^{-i(k_x x+\theta)}\right) \\ Ce^{ik_x x} + De^{-ik_x x} \\ s\left(Ce^{i(k_x x-\theta)} - De^{-i(k_x x-\theta)}\right) \end{pmatrix}, \tag{3.1}$$

where $k_x^2 = \varepsilon^2/\hbar^2 v^2 - k_y^2$, $e^{i\theta} = (k_x + ik_y)/\sqrt{k_x^2 + k_y^2}$, $s = \varepsilon/|\varepsilon|$, and A, B, C and D are numbers to be determined by satisfying the boundary condition, as we will argue in the following.

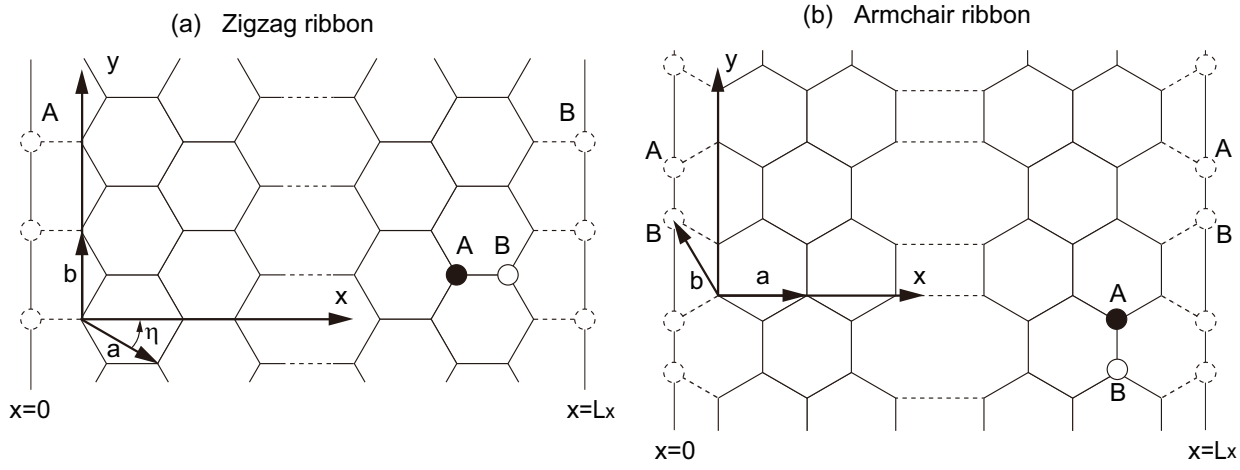

Figure 3.1: Atomic structures of graphene ribbons with (a) zigzag boundary and (b) armchair boundary, respectively. Dashed circles indicate missing sites beyond the boundary.

3.1.2 Zigzag boundary

In the zigzag ribbon, the boundary condition is given by $\psi_{\rm A}(\boldsymbol{R}_{\rm A}) = 0$ at $x = 0$, and $\psi_{\rm B}(\boldsymbol{R}_{\rm B}) = 0$ at $x = L_x$. By using Eq.(2.17), this is translated to the condition for the envelope function as

$$\begin{aligned} F_{\rm A}^{\rm K}(0, y) &= 0, \\ F_{\rm B}^{\rm K}(L_x, y) &= 0, \\ F_{\rm A}^{\rm K'}(0, y) &= 0, \\ F_{\rm B}^{\rm K'}(L_x, y) &= 0, \end{aligned} \tag{3.2}$$

which keeps the states at K and those at K′ independent. For an eigenstate for the K point, we apply the first two lines of Eq.(3.2) to Eq.(3.1), to obtain

$$\begin{aligned} &A + B = 0, \\ &s\left(Ae^{i(k_x L_x + \theta)} - Be^{-i(k_x L_x + \theta)}\right) = 0. \end{aligned} \tag{3.3}$$

To have a solution other than $A = B = 0$, we require [31]

$$k_y = \frac{k_x}{\tan k_x L_x}. \tag{3.4}$$

For given k_y, we define $k_n (n = 0, 1, 2, \cdots)$ as solution of Eq.(3.4) in k_x satisfying $n\pi < k_n L_x < (n+1)\pi$. Corresponding eigenstates and the energy are obtained as

$$\begin{aligned} \boldsymbol{F}_{snk_y}(\boldsymbol{r}) &= A_n \frac{e^{ik_y y}}{\sqrt{L_x L_y}} \begin{pmatrix} i \sin k_n x \\ s(-1)^{n+1} \sin k_n (x - L_x) \\ 0 \\ 0 \end{pmatrix}, \\ A_n &= \left(1 - \frac{\sin 2k_n L_x}{2k_n L_x}\right)^{-1/2}, \\ \varepsilon_{snk_y} &= s\hbar v \sqrt{k_n^2 + k_y^2}, \end{aligned} \tag{3.5}$$

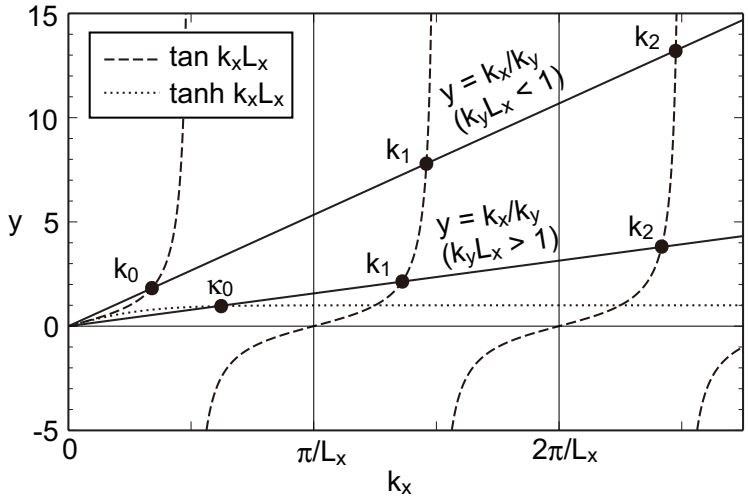

Figure 3.2: Plots to find solutions of Eq.(3.4) and Eq.(3.6).

for $n = 0, 1, 2, \cdots$. For the normalization of the wavefunction, we assumed the periodic boundary condition in y-direction with a large enough period L_y.

Solution k_n is obtained by searching for crossing points of $\tan k_x L_x$ and k_x/k_y as illustrated in Fig. 3.2. When $k_y L_x > 1$, the first solution k_0 becomes a pure imaginary number $i\kappa_0$ which satisfies

$$k_y = \frac{\kappa_0}{\tanh \kappa_0 L_x}. \tag{3.6}$$

The wavefunction and the energy then becomes

$$\begin{aligned}
\boldsymbol{F}_{s0k_y}(\boldsymbol{r}) &= A_0 \frac{e^{ik_y y}}{\sqrt{L_x L_y}} \begin{pmatrix} i \sinh \kappa_0 x \\ -s \sinh \kappa_0 (x - L_x) \\ 0 \\ 0 \end{pmatrix}, \\
A_0 &= \left(-1 + \frac{\sinh 2\kappa_0 L_x}{2\kappa_0 L_x} \right)^{-1/2}, \\
\varepsilon_{s0k_y} &= s\hbar v \sqrt{-\kappa_0^2 + k_y^2}.
\end{aligned} \tag{3.7}$$

This actually describes the edge state localized at the boundary $x = 0$ and L_x giving a nearly flat energy band. [25, 27, 28]

The eigenenergy ε_{snk_y} represents the n-th branch of conduction ($s = +$) and valence ($s = -$) bands respectively. Energy band structure of K as a function of k_y is shown as solid curves in Fig. 3.3(a). Eigenstates for K′ point are obtained similarly, where the energy band structure is equivalent to Fig. 3.3(a) with k_y inverted to $-k_y$. The flat band of edge states of K and K′ are connected in a wave number away from K or K′. [25, 27, 28]

3.1.3 Armchair boundary

In the armchair ribbon, the boundary condition imposes both of $\psi_{\mathrm{A}}(\boldsymbol{R}_{\mathrm{A}}) = 0$ and $\psi_{\mathrm{B}}(\boldsymbol{R}_{\mathrm{B}}) = 0$ at each of $x = 0$ and $x = L_x$. The corresponding conditions for the envelope functions are written as

$$\begin{aligned}
F_{\mathrm{A}}^{\mathrm{K}}(0, y) + F_{\mathrm{A}}^{\mathrm{K}'}(0, y) &= 0, \\
F_{\mathrm{B}}^{\mathrm{K}}(0, y) - F_{\mathrm{B}}^{\mathrm{K}'}(0, y) &= 0, \\
F_{\mathrm{A}}^{\mathrm{K}}(L_x, y) + \omega^{-2N} F_{\mathrm{A}}^{\mathrm{K}'}(L_x, y) &= 0, \\
F_{\mathrm{B}}^{\mathrm{K}}(L_x, y) - \omega^{-2N} F_{\mathrm{B}}^{\mathrm{K}'}(L_x, y) &= 0,
\end{aligned} \tag{3.8}$$

where $N = L_x/a$ is the number of honeycomb lattices between $x = 0$ and L_x, which can be integer or half-integer depending on the position of the edge.

Applying above conditions to Eq.(3.1), we obtain

$$\begin{pmatrix} 1 & 1 & 1 & 1 \\ e^{i\theta} & -e^{-i\theta} & -e^{-i\theta} & e^{i\theta} \\ e^{i\lambda} & e^{-i\lambda} & \alpha e^{i\lambda} & \alpha e^{-i\lambda} \\ e^{i(\lambda+\theta)} & -e^{-i(\lambda+\theta)} & -\alpha e^{i(\lambda+\theta)} & \alpha e^{-i(\lambda+\theta)} \end{pmatrix} \begin{pmatrix} A \\ B \\ C \\ D \end{pmatrix} = \begin{pmatrix} 0 \\ 0 \\ 0 \\ 0 \end{pmatrix}, \tag{3.9}$$

where $\alpha = \omega^{-2N}$ and $\lambda = k_x L_x$. The determinant of matrix in Eq.(3.9) should vanish to have a non-zero solution. This condition is reduced to

$$k_x = k_n \equiv \frac{\pi}{L_x} \left(n - \frac{\nu}{3} \right), \ n = 0, \pm 1, \pm 2, \cdots, \tag{3.10}$$

ν is an integer $(0, \pm 1)$ defined by

$$2N = 3m + \nu, \tag{3.11}$$

with integer m. The eigenstate and energy are obtained as

$$\boldsymbol{F}_{snk_y}(\boldsymbol{r}) = \frac{e^{ik_y y}}{2\sqrt{L_x L_y}} \begin{pmatrix} e^{ik_n x} \\ s e^{i(k_n x + \theta)} \\ -e^{-ik_n x} \\ s e^{-i(k_n x - \theta)} \end{pmatrix},$$
$$\varepsilon_{snk_y} = s\hbar v \sqrt{k_n^2 + k_y^2}. \tag{3.12}$$

When $\nu = 0$, the energy bands of $n = 0$ and $s = \pm$ stick together and thus the system is metallic, while otherwise a gap opens at zero energy and the system becomes a semiconductor. Energy bands for metallic armchair ribbon ($\nu = 0$) and semiconducting armchair ribbon ($\nu = \pm 1$) are shown in Fig. 3.3(b) and (c), respectively. In (c), the labeling n is for the case of $\nu = +1$, while n becomes $-n$ in $\nu = -1$.

3.1.4 Orbital susceptibility

To calculate the orbital diamagnetism, we consider a graphene ribbon under a uniform magnetic field B perpendicular to graphene plane. We take the Landau gauge and set the vector potential as

$$\boldsymbol{A}(\boldsymbol{r}) = \left[0,\, B\left(x - \frac{L_x}{2}\right)\right]. \tag{3.13}$$

The Hamiltonian in presence of the magnetic field is obtained by replacing $\hat{\boldsymbol{k}}$ by $\hat{\boldsymbol{k}} + e\boldsymbol{A}/(\hbar c)$, as

$$\mathcal{H} = \mathcal{H}_0 + \delta\mathcal{H}, \quad \delta\mathcal{H} = \frac{e}{c}\hat{v}_y A_y, \tag{3.14}$$

where c is the light velocity, and

$$\hat{v}_y = \frac{1}{\hbar}\frac{\partial \mathcal{H}}{\partial \hat{k}_y} = v \begin{pmatrix} 0 & -i & 0 & 0 \\ i & 0 & 0 & 0 \\ 0 & 0 & 0 & i \\ 0 & 0 & -i & 0 \end{pmatrix}. \tag{3.15}$$

The operator of the electric current density is given by

$$\hat{j}_y(\boldsymbol{r}) = -\frac{e}{2}\left\{\hat{v}_y \delta(\boldsymbol{r} - \boldsymbol{r}') + \delta(\boldsymbol{r} - \boldsymbol{r}')\hat{v}_y\right\}. \tag{3.16}$$

In the first order perturbation in $\delta\mathcal{H}$, the expectation value of the current density is written as

$$j_y(\boldsymbol{r}) = \sum_\alpha f(\varepsilon_\alpha) \sum_{\beta(\neq\alpha)} \frac{2\mathrm{Re}\left[(\delta\mathcal{H})_{\alpha\beta}(\hat{\mathrm{j}}_\mathrm{y}(\mathrm{r}))_{\beta\alpha}\right]}{\varepsilon_\alpha - \varepsilon_\beta}, \tag{3.17}$$

where α and β represent the unperturbed eigenstates of graphene ribbon, and $f(\varepsilon)$ is the Fermi distribution function.

In a zigzag ribbon, the current density always vanishes at the edges $x = 0$ and L_x, while it is not generally the case in armchair ribbons. This is obvious from at the matrix element of $\hat{j}_y$ between two eigen states $\boldsymbol{F}$ and $\boldsymbol{F}'$,

$$\langle \boldsymbol{F}'|\hat{j}_y(\boldsymbol{r})|\boldsymbol{F}\rangle = iev\left[F'K_{\rm A}(\boldsymbol{r})^* F^{\rm K}_{\rm B}(\boldsymbol{r}) - F'K_{\rm B}(\boldsymbol{r})^* F^{\rm K}_{\rm A}(\boldsymbol{r})\right]. \tag{3.18}$$

In the wavefunction of zigzag ribbon, Eqs. (3.5) and (3.7), the component $F^{\rm K}_{\rm A}$ is zero at $x = 0$, and $F^{\rm K}_{\rm B}$ is at L_x, so that Eq. (3.18) vanishes at the both edges.

The current density on xy-plane is related to the local magnetic moment $m(\boldsymbol{r})$ in z-direction by

$$j_x = c\frac{\partial m}{\partial y},\ j_y = -c\frac{\partial m}{\partial x}. \tag{3.19}$$

In the present case, $m(\boldsymbol{r})$ depends only on x so that the total magnetization per area is

$$\begin{aligned} M &= \frac{1}{L_x L_y}\int_0^{L_x}\int_0^{L_y} m(x)\mathrm{d}x\mathrm{d}y \\ &= \frac{1}{cL_x}\int_0^{L_x}\left(x - \frac{L_x}{2}\right) j_y(x)\mathrm{d}x. \end{aligned} \tag{3.20}$$

The magnetic susceptibility is written as

$$\chi = \lim_{B\to 0}\frac{M}{B} = \frac{2}{cL_xL_y}\sum_\alpha f(\varepsilon_\alpha)\sum_{\beta(\neq\alpha)}\frac{\left|(\delta\mathcal{H}/B)_{\alpha\beta}\right|^2}{\varepsilon_\beta - \varepsilon_\alpha}. \tag{3.21}$$

We calculate Eqs. (3.17) and (3.21) numerically. As we have infinite energy bands below zero, we introduce a cut-off function $C(\varepsilon_\alpha)$ which smoothly vanishes $|\varepsilon_\alpha| > \varepsilon_c$. In the following, we take $\varepsilon_c = 50\varepsilon_0$ where

$$\varepsilon_0 = \frac{2\pi\hbar v}{L_x} \tag{3.22}$$

is the typical energy scale for the subband structure. The result is actually converging in the limit of large ε_c.

In the graphene ribbon, the characteristic unit of the susceptibility can be chosen as

$$\chi_0 = g_v g_s \frac{e^2v^2}{6\pi c^2}\frac{1}{\varepsilon_0}. \tag{3.23}$$

3.2 Numerical Results

3.2.1 Magnetic susceptibility

Lower panels of Fig.3.3 show the orbital susceptibility $\chi(\varepsilon_{\rm F})$ of (a) zigzag, (b) metallic armchair ($\nu = 0$) and (c) semiconducting armchair ($\nu = \pm 1$) ribbons at zero temperature, where the upward direction represents the negative (i.e., diamagnetic) susceptibility. The figures are to be compared with the band structures in upper panels. In every case, the magnitude of χ becomes the maximum at $\varepsilon_{\rm F} = 0$, and oscillates as a function of $\varepsilon_{\rm F}$ in accordance with the subband structure. In the positive energy region, for example, the curve sharply rises when a subband starts to be occupied by electrons, while it tends

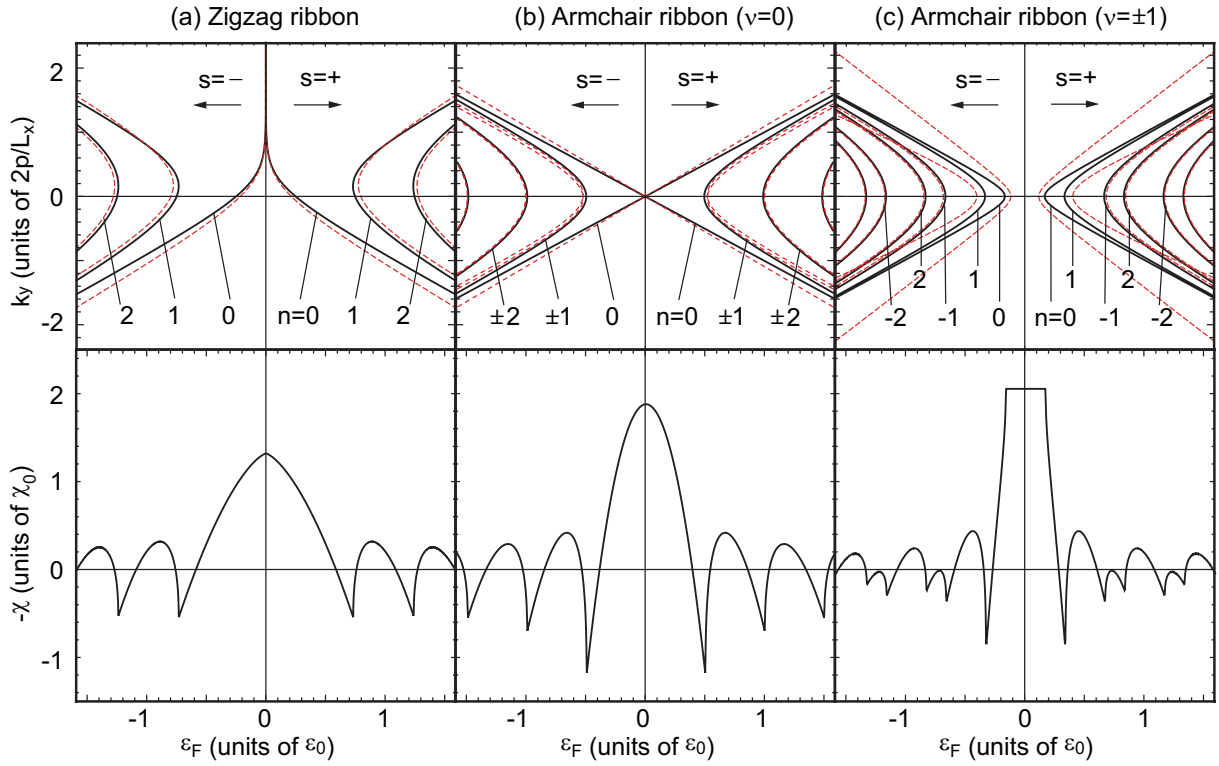

Figure 3.3: Band structure (upper panel) and magnetic susceptibility as a function of $\varepsilon_{\rm F}$ (lower), of (a) zigzag, (b) metallic armchair ($\nu = 0$) and (c) semiconducting armchair ($\nu = \pm 1$) graphene ribbons. In upper panels, solid (black) and dashed (red) curves indicate the band structures at zero and a finite magnetic field, respectively. For the latter, the energy band is calculated with the perturbation theory in a magnetic field B. where we take $B = B_0$ for (a), and $B = 0.5B_0$ in (b) and (c) for illustrative purpose, and $B_0 = (ch/e)/L_x^2$.

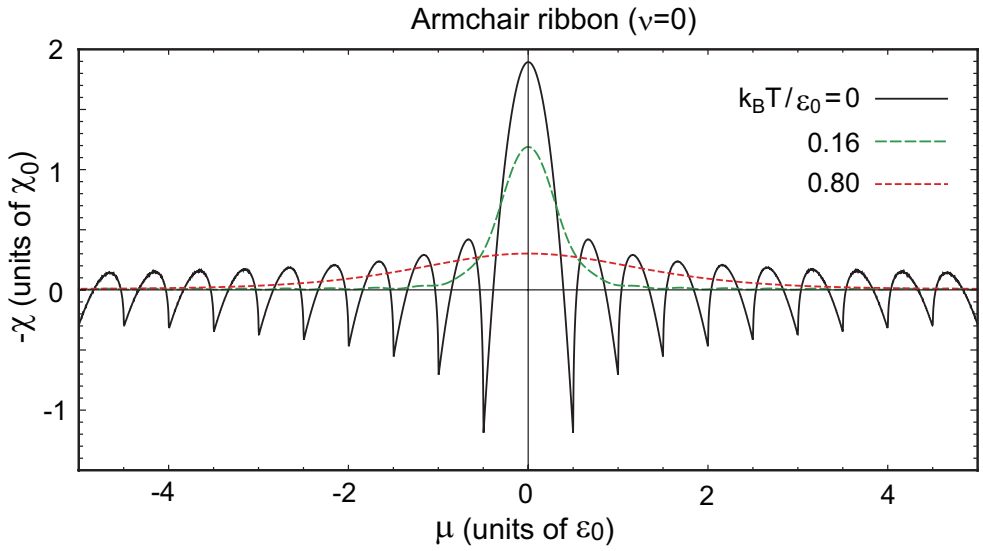

Figure 3.4: Magnetic susceptibility against chemical potential μ for metallic armchair ribbon ($\nu = 0$) at several different temperatures.

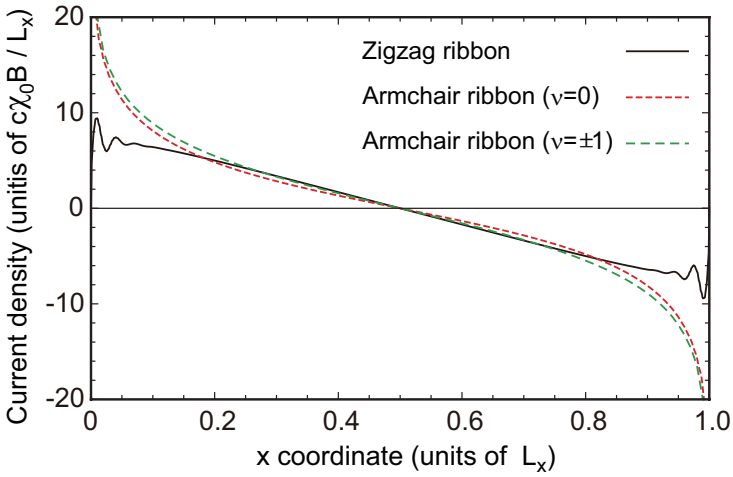

Figure 3.5: Diamagnetic current density $j_y(x)$ of different types of graphene ribbons with $\varepsilon_{\rm F} = 0$ at $T = 0$.

to decrease otherwise. In large $|\varepsilon_{\rm F}|$, the amplitude of the oscillation slowly attenuates approximately in proportional to $1/\sqrt{|\varepsilon_{\rm F}|}$.

The oscillating feature can be understood in terms of the band energy shift in an infinitesimal magnetic field. In the upper figures of Fig. 3.3, we plot as broken curves the energy band in some small B calculated by the second order perturbation. Here the amplitude B is set to some finite value for illustrative purpose. Generally the system is diamagnetic when the total energy shift caused by B is positive, and paramagnetic when negative. In the metallic armchair ribbon (b), for example, we see that a pair of the first subbands ($n = 0, s = \pm$) shift towards zero energy, due to the level repulsions from excited subbands nearby. All other bands ($|n| \geq 1$) move in the opposite direction away from zero energy, while the absolute shifts are much smaller than that of $n = 0$.

When $\varepsilon_{\rm F}$ is zero, the energy gain of the first valence band ($s = -, n = 0$) exceeds the energy loss of all other valence bands ($s = -, |n| \geq 1$), resulting in the total diamagnetism. When ε_F is shifted to positive side, the diamagnetism decreases because the first conduction band ($s = +, n = 0$) has a negative shift and gives paramagnetism. When the second conduction band ($s = +, |n| = 1$) starts to be filled, the susceptibility suddenly jumps to diamagnetic direction, because the shift is positive there and also the density of states diverges at the band bottom. The oscillation of other types, (a) and (c), can be explained in a similar manner.

In Fig. 3.4, the susceptibility at several different temperatures is plotted as a function of the chemical potential μ. We here choose the metallic armchair ribbon ($\nu = 0$) while the qualitative property is the same in other cases. We see that the oscillation rapidly disappears once $k_{\rm B}T$ becomes of the order of ε_0, i.e., the thermal broadening energy is as large as the subband interval energy, and we are left with only a single diamagnetic peak at $\varepsilon_{\rm F} = 0$. When $k_{\rm B}T \gtrsim \varepsilon_0$, the curve becomes almost identical with the bulk susceptibility, Eq. (2.38), or the thermally-broadened delta function. When we fix the temperature and increase the ribbon width instead, we would see that the oscillatory curve of $\chi(\mu)$ is shrinking in the horizontal direction as the energy scale ε_0 decreases, and, once ε_0 becomes as small as $k_{\rm B}T$, the oscillation vanishes and the curve goes to the bulk limit. Similar behavior is observed in all the types of ribbons considered here, and the finite size effect always disappears when $k_{\rm B}T \gtrsim \varepsilon_0$ regardless of the edge configuration.

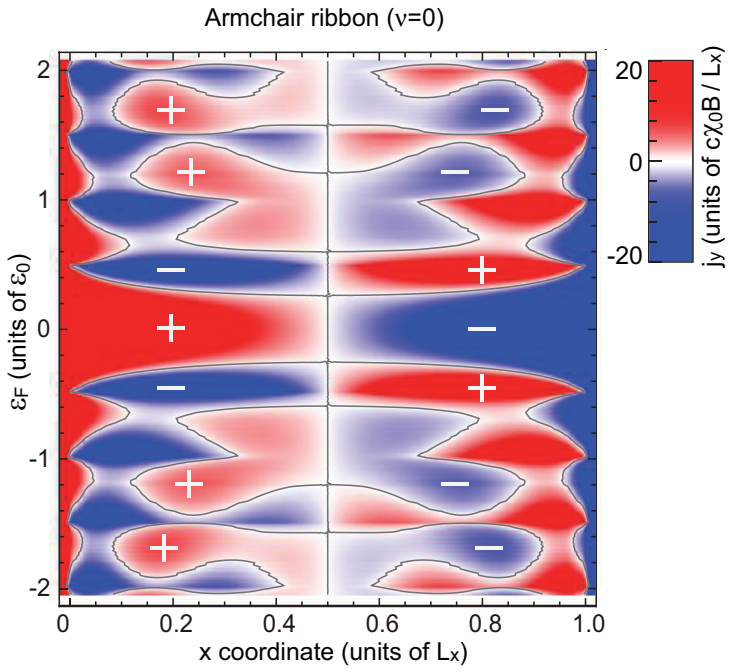

Figure 3.6: Two-dimensional density plot $j_y(x;\varepsilon_{\rm F})$ of the diamagnetic current density of metallic armchair ribbon ($\nu = 0$), as a function of position x (horizontal axis) and Fermi energy (vertical).

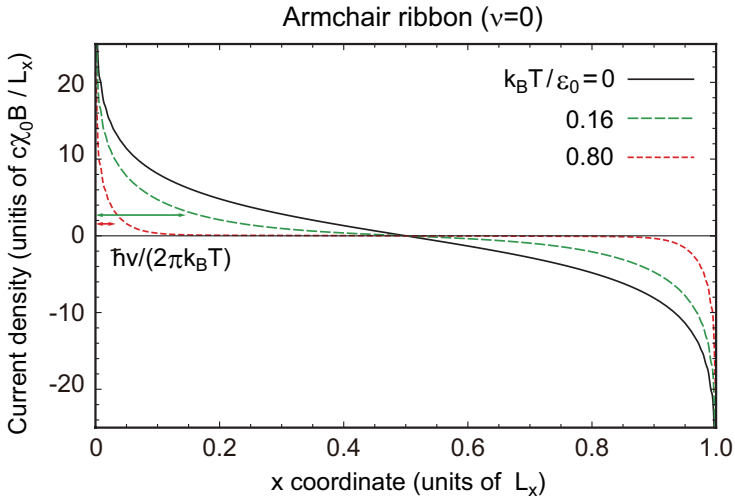

Figure 3.7: Diamagnetic current density $j_y(x)$ of metallic armchair ribbon ($\nu = 0$) with $\varepsilon_{\rm F} = 0$, at several different temperatures. The vertical arrows indicate the characteristic length scale $\hbar v/(2\pi k_{\rm B}T)$ measured from $x = 0$.

3.2.2 Diamagnetic current density

Fig. 3.5 shows the diamagnetic current density $j_y(x)$ in different types of graphene ribbons at $\varepsilon_{\rm F} = 0$ and $T = 0$, calculated in the first order perturbation of B. The unit of current density is taken as $c\chi_0 B/L_x$. The current flows in opposite directions in the left-hand side and right-hand side of the ribbon, to make a magnetization perpendicular to the layer. Reflecting the absence of the characteristic length scale, the current distribution is not localized to the edge but spread in the entire width in a form of slowly-varying monotonic function.

In zigzag ribbons, the current density actually becomes absolute zero at $x = 0$ and L_x, in accordance with the constraint argued in the previous section. The current sharply drops to zero at the edges, and some oscillatory feature remains around the edge due to a finite cut-off energy. When we increase the energy cut-off (not shown), the curve appears to slowly approach a fixed curve having a discontinuous jump at the edges. In the armchair ribbons, j_y is not necessarily zero but logarithmically diverges at the both edges. The numerical calculation converges much more rapidly there, since there is no discontinuity as in the zigzag case.

Fig. 3.6 is the two-dimensional density plot $j_y(x;\varepsilon_{\rm F})$ of the diamagnetic current density of metallic armchair ribbon, as a function of position x (horizontal axis) and Fermi energy (vertical). In increasing $\varepsilon_{\rm F}$, the current distribution begins to oscillate as a function of x, with a characteristic wave number of the order of $k_{\rm F} = \varepsilon_{\rm F}/(\hbar v)$.

The temperature dependence of the current density at $\mu = 0$ is shown in Fig.3.7 for the same metallic armchair ribbon. When $k_{\rm B}T$ becomes as large as ε_0, the current distribution is localized at the boundary forming the counter edge currents. This is the same temperature range where the oscillation of χ disappears and the bulk limit is achieved. The depth of the current distribution is characterized by

$$\lambda_{\rm edge}(T) = \frac{\hbar v}{2\pi k_{\rm B} T}, \tag{3.24}$$

which shrinks in increasing temperature. With the band velocity of graphene, $v \approx 10^6$ m/s, it is estimated as $\lambda_{\rm edge} \approx [1/T(K)]\mu$m.

This behavior is intuitively explained using the plot of $j_y(x;\varepsilon_{\rm F})$ in Fig.3.6. The current density at a finite T is obtained by integrating $j_y(x;\varepsilon_{\rm F})$ in $\varepsilon_{\rm F}$ with the thermal averaging factor $-\partial f/\partial\varepsilon$. The current of the middle part of the ribbon vanishes in averaging the oscillating function in $\varepsilon_{\rm F}$, while the cancellation is not complete only near the edges, since j_y is always positive and negative in left and right ends, respectively. The similar temperature dependence of the current distribution is found in other types of ribbons considered here. This suggests that, in any finite pieces of graphene with length scale L, the finite-size effect disappears when $k_{\rm B}T \gtrsim \varepsilon_0$, and then the diamagnetic current circulates only near edge with a depth $\lambda_{\rm edge}$. This is actually confirmed for graphene flakes in Chapter. 3.

The diamagnetic current distribution in graphene is significantly different from conventional electron system. In Appendix B, we calculate the current distribution in a ribbon of usual two-dimensional electron gas, where we will see that the diamagnetic current is always localized near the edge with a depth of the Fermi wavelength, as long as the Fermi energy is much larger than $k_{\rm B}T$.

3.2.3 Relation to spin paramagnetism

We neglect the effect of the electron spin through out the present analysis. In a zigzag ribbon, particularly, the large density of states contributed by the zero-energy flat band is

expected to give a significant magnitude of Pauli paramagnetism and reduce the orbital diamagnetism. [28]

The ratio between two effects can be quantitatively estimated as follows. The susceptibility of Pauli paramagnetism is given by

$$\chi_{\rm para} = \left(\frac{g}{2}\right)\mu_{\rm B}^2 D(\varepsilon), \tag{3.25}$$

where $g \sim 2$ is the g-factor for graphene electron, $\mu_{\rm B} = e\hbar/(2mc)$ is the Bohr-magneton with m being the free-electron mass, and $D(\varepsilon)$ is the density of states per area given by the zero-energy flat band. Since the number of edge states accommodated in a ribbon of the length L is $\sim L/a$ per spin and per valley, [28] we have

$$D(\varepsilon) \sim \frac{g_{\rm v} g_{\rm s}}{L^2}\frac{L}{a}\delta(\varepsilon), \tag{3.26}$$

which gives a delta-function singularity in $\chi_{\rm para}$.

By comparing $\chi_{\rm para}$ with the bulk orbital diamagnetism $\chi_{\rm Dirac}$, Eq. (2.38), we obtain

$$\left|\frac{\chi_{\rm para}}{\chi_{\rm Dirac}}\right| = \frac{3\pi}{2}\frac{\hbar^2}{m^2 v^2 a L} \sim 1.0 \times \frac{a}{L}, \tag{3.27}$$

which is negligible in a wide strip with $L \gg a$. In a low temperature such that $k_{\rm B}T \lesssim \varepsilon_0$, however, $\chi_{\rm Dirac}$ cannot be regarded as thermally broadened delta-function due to the effect of the subband formation, and then $\chi_{\rm para}$ overcomes $\chi_{\rm Dirac}$ only at $\varepsilon_{\rm F} = 0$.

3.3 Carbon Nanotubes

The carbon nanotube is a quasi-one-dimensional system similar to graphene ribbon, but different in that there are no edges. [72, 73] Experimentally, graphene nanoribbons with smooth edges can be obtained by unzipping the carbon nanotubes, i.e., lengthwise cutting of carbon nanotube side walls. [20, 21] Then we may ask which of the ribbon and the original nanotube has greater diamagnetism, and how the susceptibility oscillation in $\varepsilon_{\rm F}$ changes in unzipping. The orbital susceptibility of carbon nanotube was theoretically studied for small Fermi energies in the effective mass approximation [60, 61]. Here we compute full Fermi energy dependence in parallel fashion to the analysis for ribbons.

A carbon nanotube is characterized by a chiral vector,

$$\boldsymbol{L} = n_a \boldsymbol{a} + n_b \boldsymbol{b}, \tag{3.28}$$

where the atom at $\boldsymbol{L}$ on a graphene sheet is rolled up onto the origin in constructing a tube. The boundary condition is given by $\psi_{\rm A}(\boldsymbol{R}_{\rm A}) = \psi_{\rm A}(\boldsymbol{R}_{\rm A} + \boldsymbol{L})$ and $\psi_{\rm B}(\boldsymbol{R}_{\rm B}) = \psi_{\rm B}(\boldsymbol{R}_{\rm B} + \boldsymbol{L})$. For the effective mass wavefunction, it is written as [9]

$$\begin{aligned}
\boldsymbol{F}^{\rm K}(\boldsymbol{r} + \boldsymbol{L}) &= \exp\left(-\frac{2\pi i}{3}\nu\right)\boldsymbol{F}^{\rm K}(\boldsymbol{r}), \\
\boldsymbol{F}^{\rm K'}(\boldsymbol{r} + \boldsymbol{L}) &= \exp\left(+\frac{2\pi i}{3}\nu\right)\boldsymbol{F}^{\rm K'}(\boldsymbol{r}).
\end{aligned} \tag{3.29}$$

Here $\boldsymbol{F}^{\rm K} = (F_{\rm A}^{\rm K}, F_{\rm B}^{\rm K})$ etc., and ν is an integer $(0, \pm 1)$ defined by

$$n_a + n_b = 3m + \nu, \tag{3.30}$$

with integer m.

For K point, the eigenstates are immediately obtained as

$$\boldsymbol{F}^{\mathrm{K}}_{snk_y}(\boldsymbol{r}) = \frac{e^{ik_y y}}{\sqrt{2L_xL_y}} \begin{pmatrix} e^{ik_n x} \\ se^{i(k_n x+\theta)} \\ 0 \\ 0 \end{pmatrix},$$
$$\varepsilon_{snk_y} = s\hbar v\sqrt{k_y^2+k_n^2}, \tag{3.31}$$

where

$$k_n \equiv \frac{2\pi}{L_x}\left(n-\frac{\nu}{3}\right),\ n=0,\pm1,\pm2,\cdots, \tag{3.32}$$

and $L_x = |\boldsymbol{L}|$ and L_y is length of the carbon nanotube. The system is metallic when $\nu = 0$, and semiconducting when $\nu = \pm 1$. The band structure looks similar to armchair graphene ribbon's, but the unit of momentum quantization doubled compared to Eq. (3.10), leading to wider energy spacing between subbands. The energy band for K′ is obtained by replacing k_y by $-k_y$ and also ν by $-\nu$.

When a uniform magnetic field B is applied perpendicularly to the nanotube axis, the vector potential can be taken as

$$\boldsymbol{A}(\boldsymbol{r}) = \left(0,\ \frac{BL_x}{2\pi}\sin\frac{2\pi x}{L_x}\right). \tag{3.33}$$

We should note that the expression differs from that for ribbon, Eq. (3.13), because the magnetic field perpendicular to the tube surface is not a constant, but a sinusoidal function in x. Except for that, the magnetic susceptibility $\chi_{\mathrm{tube}}(\varepsilon_{\mathrm{F}})$ is calculated in the same formula, Eq. (3.21).

The susceptibility of the carbon nanotube is naturally related to that of graphene against a spatial varying magnetic field $B(q)\sin qx$ with $q = 2\pi/L_x \equiv q_0$. When we define the q-dependent susceptibility of graphene as $\chi_{\mathrm{Dirac}}(q) \equiv m(q)/B(q)$, [57] we obtain a relation

$$\langle\chi_{\mathrm{tube}}(\varepsilon_F)\rangle_\varphi = \frac{1}{2}\chi_{\mathrm{Dirac}}(q_0;\varepsilon_F). \tag{3.34}$$

Here $\langle\,\rangle_\varphi$ represents an average over a phase factor φ which twists the boundary condition of carbon nanotube as $\psi(\boldsymbol{r}+\boldsymbol{L}) = \exp(2\pi i\varphi)\psi(\boldsymbol{r})$. Physically, the phase factor corresponds to threading a magnetic flux of $(ch/e)\varphi$ into the nanotube cross section.[9, 60] It changes momentum quantization of Eq. (3.32) to $k_n = (2\pi/L_x)(n+\varphi-\nu/3)$, and the flux averaging over φ smears the difference in ν. The factor 1/2 in Eq. (3.34) enters because the average of the squared magnetic field on the nanotube surface is $B(q_0)^2/2$.

At the zero temperature, $\chi_{\mathrm{Dirac}}(q;\varepsilon_{\mathrm{F}})$ is explicitly evaluated as [57]

$$\begin{aligned}\chi_{\mathrm{Dirac}}(q;\varepsilon_{\mathrm{F}}) &= -\frac{g_{\mathrm{v}}g_{\mathrm{s}}e^2v}{16\hbar c^2}\frac{1}{q}\,\theta(q-2k_{\mathrm{F}}) \\ &\quad\times\left[1+\frac{2}{\pi}\frac{2k_{\mathrm{F}}}{q}\sqrt{1-\left(\frac{2k_{\mathrm{F}}}{q}\right)^2}-\frac{2}{\pi}\sin^{-1}\frac{2k_{\mathrm{F}}}{q}\right],\end{aligned} \tag{3.35}$$

where $k_{\mathrm{F}} = |\varepsilon_{\mathrm{F}}|/(\hbar v)$ is the Fermi wave number and $\theta(x)$ is defined by $\theta(x) = 1\,(x>0)$ and $0\,(x<0)$. Using Eqs. (3.34) and (3.35), the flux-averaged susceptibility integrate is

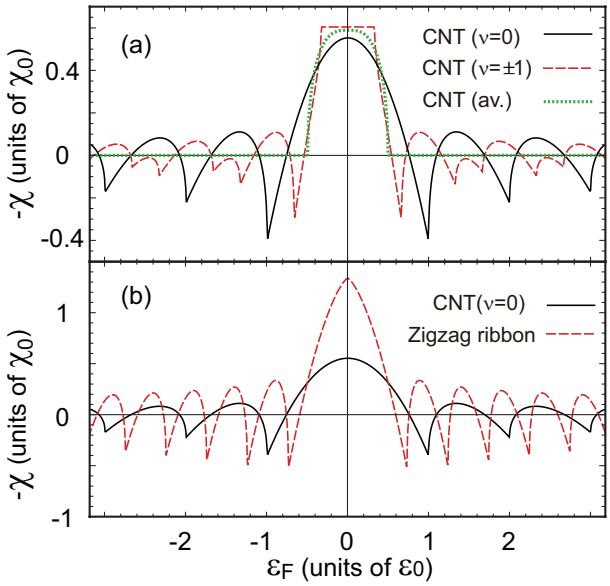

Figure 3.8: (a) Magnetic susceptibility of carbon nanotubes. Solid (black), dashed (red) and dotted (green) curves are for metallic ($\nu = 0$), semiconducting ($\nu = \pm 1$), and the flux average, respectively. (b) Magnetic susceptibility of the carbon nanotube of $\nu = 0$ (solid black) and the zigzag ribbon unzipped from the same nanotube (dashed red).

shown to be

$$\left\langle \int_{-\infty}^{\infty} \chi_{\rm tube}(\varepsilon_F) d\varepsilon_F \right\rangle_{\varphi} = \frac{1}{2}\left(-g_v g_s \frac{e^2 v^2}{6\pi c^2}\right), \tag{3.36}$$

which is exactly half of graphene's, suggesting that the susceptibility is effectively smaller in nanotube than in ribbon. This is simply because the B-field component penetrating the lattice plane is smaller in the nanotube due to its cylindrical shape.

The susceptibility before taking flux average can be calculated in numerics. Fig. 3.8 (a) shows $\chi_{\rm tube}(\varepsilon_{\rm F})$ for the metallic ($\nu = 0$) and the semiconducting ($\nu = \pm 1$) nanotubes, together with the flux average. It has an oscillatory behavior similar to the graphene ribbon's, while χ in $|\varepsilon_{\rm F}| > \hbar v q/2$ completely vanishes after flux average.[57] In increasing temperature (not shown), the oscillation immediately disappears, leaving a single peak regardless of ν, similar to the graphene ribbon.

Fig. 3.8 (b) compares the susceptibility of a carbon nanotube and that of corresponding graphene ribbon unzipped from the same nanotube. Here we chose a zigzag ribbon as an example, when the corresponding nanotube becomes an armchair nanotube which is always metallic ($\nu = 0$). [9] The oscillation period of the nanotube is approximately twice as large as that of the ribbon, reflecting the wider subband spacing. Overall magnitude of χ is smaller in nanotube roughly by factor 2. The integrate of susceptibility in $\varepsilon_{\rm F}$ differs in factor 2 in numerical accuracy, in accordance with the above arguments.

Chapter 4

Graphene Flakes

4.1 Formulations

In this chapter, we consider four different atomic configurations of graphene flakes as shown in Fig. 4.1, which are characterized by hexagonal or trigonal global shapes and by armchair or zigzag edge termination. For each case, we range the system size from a few nm to a few tens of nm. We describe the motion of graphene electrons using the nearest-neighbor tight-binding model of p_z orbitals. The Hamiltonian is written as

$$H = -\gamma_0 \sum_{\langle n,m \rangle} e^{i2\pi\phi_{nm}} c_n^\dagger c_m, \tag{4.1}$$

where $c_n^\dagger$ is the creation operator of π electron at the site n, and $\langle n, m \rangle$ represents summation over all nearest-neighbor sites. The system is under a uniform magnetic field $\boldsymbol{B}$

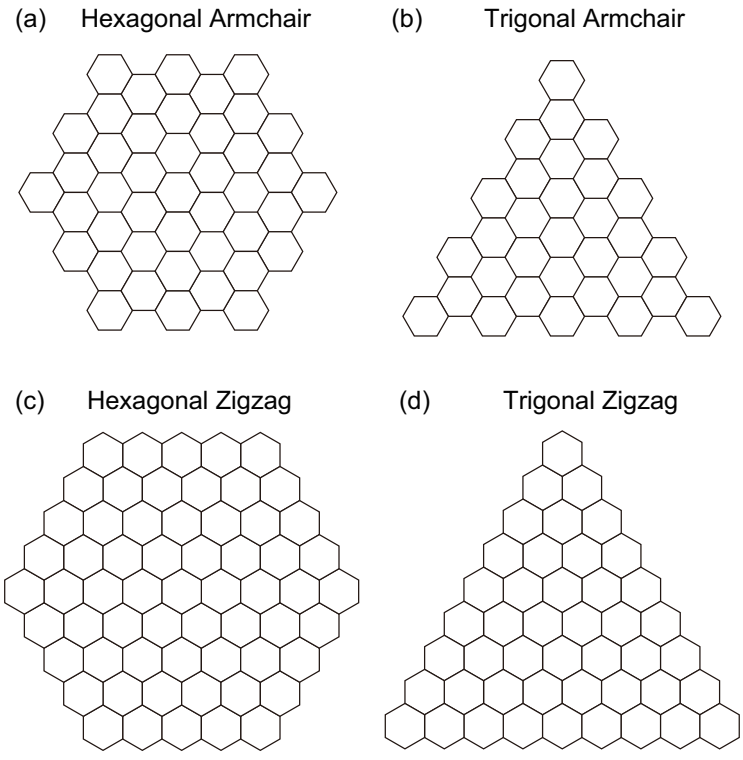

Figure 4.1: Atomic structures of graphene flakes with (a) hexagonal armchair, (b) trigonal armchair, (c) hexagonal zigzag, and (d) trigonal zigzag flake.

perpendicular to the graphene plane, which is incorporated by the Peierls phase ϕ_{nm},

$$\phi_{nm} = \frac{e}{ch} \int_n^m \mathrm{d}\boldsymbol{\ell} \cdot \boldsymbol{A}, \tag{4.2}$$

where $\boldsymbol{A}(\boldsymbol{r})$ is the vector potential giving the magnetic field by $\boldsymbol{B} = \nabla \times \boldsymbol{A}$.

For each single graphene flake, we diagonalize Hamiltonian Eq. (4.1) and obtain a set of eigenenergies ε_i. The thermodynamical potential at temperature T and chemical potential μ is written as

$$\Omega = -k_{\mathrm{B}}T \sum_i \ln\left\{1 + \exp[(\mu - \varepsilon_i)/k_{\mathrm{B}}T]\right\}. \tag{4.3}$$

The magnetic susceptibility is given by

$$\chi = -\frac{1}{S}\left(\frac{\partial^2 \Omega}{\partial B^2}\right)_{\mu,T}\Bigg|_{B=0}, \tag{4.4}$$

where S is an area of the system. To calculate this, we derive the eigenenergies at zero magnetic field and those at a small finite magnetic field, and numerically compute the derivative of the thermodynamic potential. The amplitude of the small field must be chosen so that the level shift from the zero field is smaller than $k_{\mathrm{B}}T$.

The electric current from site m to n is calculated by an operator,

$$J_{nm} = -i\frac{e\gamma_0}{\hbar}\left(e^{i2\pi\phi_{nm}} c_n^\dagger c_m - \mathrm{h.c.}\right). \tag{4.5}$$

We obtain the expectation value of J_{mn} for each bond using the eigenstates at a sufficiently weak magnetic field, where the current amplitude behaves linearly to B.

4.2 Magnetic susceptibility

Fig. 4.2 shows the susceptibility against the chemical potential for four types of the graphene flakes with several different temperatures. The areas of the flakes are taken to be nearly equal to $S \approx (23.5\mathrm{nm})^2$, which includes 1.1×10^4 of hexiagonal unit cells. The horizontal and vertical axes are scaled by

$$\varepsilon_0 = \frac{\hbar v}{\sqrt{S}}, \tag{4.6}$$

$$\chi_0 = \frac{g_{\mathrm{v}} g_{\mathrm{s}} e^2 v^2}{6\pi c^2 \varepsilon_0}, \tag{4.7}$$

respectively. ε_0 represents the energy scale in the Dirac cone associated with the length scale $\sqrt{S}$. We also calculated the same quantity for different system sizes (not shown) and found that for each of four types, the susceptibility and the level structure plotted in this scale becomes almost universal as long as $\sqrt{S} \gg a$. This is naturally expected from the fact that the low-energy physics are well described by the Dirac Hamiltonian.

Upper figure in each panel presents the energy level structure at $B = 0$, where dashed (black) lines are non-degenerate levels, and solid (red) lines are two-fold degenerate levels. In the low temperature regime, $k_{\mathrm{B}}T \ll \varepsilon_0$, we observe that the susceptibility abruptly changes at every single energy level, and in particular, it exhibits sharp spikes toward the paramagnetic direction (downward in the figure) at two-fold degenerate levels. This is because the degenerate states, having opposite magnetic moments, split linearly in magnetic

field just like spin Zeeman splitting, and this induces paramagnetism in an analogous way to spin Pauli paramagnetism. The contribution to the orbital suscpetibility (per area) from the degenerate states at E_0 is written as

$$\chi = \frac{2}{S} m^2 \delta(\mu - E_0), \tag{4.8}$$

where $\pm m$ is the magnetic moments of the doublet.

The major difference between armchair flakes and zigzag flakes comes from the zero-energy edge states peculiar to the zigzag edge. [35, 43] In the triangular zigzag flake, Fig. 4.2 (d), there are a number of energy levels exactly at zero energy, of which wavefunctions are shown to be localized at the edge and the degeneracy is as many as the number of edge sites of the system.[35] However, the susceptibility at $T = 0$ is completely flat there, meaning that the edge states have absolutely no contribution to the orbital magnetism. This is because the edge states are locked to zero energy even in the presence of magnetic field, and do not participate in total energy change.

In the hexiagonal zigzag flake, Fig. 4.2(c), on the other hand, the edge levels slightly shift from zero energy, because in the hexagonal case the edge states of neighboring sides are localized to different sublattices, and they are directly hybridized by the transfer integral connecting A and B sublattices. The energy shift generally depends on the magnetic field, giving some small contributions to the orbital suceptibility as actually observed in Fig. 4.2(c). Nevertheless, the edgestates do not play a significant role in the overall behavior of the orbital magnetism.

As the temperature increases, the spikes and steps in the suscpetibility are smeared out into an oscillatory curve, and in $k_{\rm B}T/\varepsilon_0 \gtrsim 1$, the oscillation eventually disappears leaving a single diamagnetic peak centered at the Dirac point. In this temperature regime, the finite-size effect is already smeared out and the plot is almost independent of the atomic configuration of the graphene flake. The central diamagentic peak in high T corresponds to the thermally-broadened delta-function in the bulk limit, Eq. (2.38).

In Fig. 4.3, we present an extended plot of the susceptibility curve of $k_{\rm B}T/\varepsilon_0 = 2.22$ in Fig. 4.2, over the whole band region. The energy axis is now scaled by absolute unit γ_0, and the temperature amounts to $k_{\rm B}T/\gamma_0 = 0.02$ in this unit. The curve is characterized by the diamagentic peak at the Dirac point, and relatively smaller structures coming from the electronic states outside the Dirac cone ($|\mu| < \gamma_0$). Specifically, we see tiny Landau diamagnetism in the quadratic band bottom at $\mu = \pm 3\gamma_0$, and paramagnetism around the van Hove singularity at $\mu = \pm\gamma_0$. [49, 58, 59] The contribution from the lower-half spectrum adds up to a paramagnetic offset to the central diamagnetic peak. Namely, the susceptibility near $\mu = 0$ is approximately written as

$$\chi(\mu; T) \approx \chi_{\rm Dirac}(\mu; T) + \chi_{\rm para}, \tag{4.9}$$

where

$$\chi_{\rm para} \approx 0.37 \times \frac{g_{\rm v} g_{\rm s} e^2 v^2}{6\pi c^2 \gamma_0}. \tag{4.10}$$

The offset $\chi_{\rm para}$ is actually negligible compared to the height of the central peak which is the order of $g_{\rm v} g_{\rm s} e^2 v^2/(24\pi c^2 k_B T)$, since $k_{\rm B}T$ is usually much smaller than γ_0.

To make the size dependence clearer, we plot in Fig. 4.4(a) and (b) $\chi(\mu = 0; T)$ of hexagonal armchair flakes with several different sizes. The panels (a) and (b) present the same information in different fashions: (a) plots χ in the absolute units γ_0 and $g_{\rm v} g_{\rm s} e^2 v^2/(6\pi c^2 \gamma_0)$ for horizontal and vertical axes, respectively, while (b) plots $\chi - \chi_{\rm para}$ i.e., the contribution

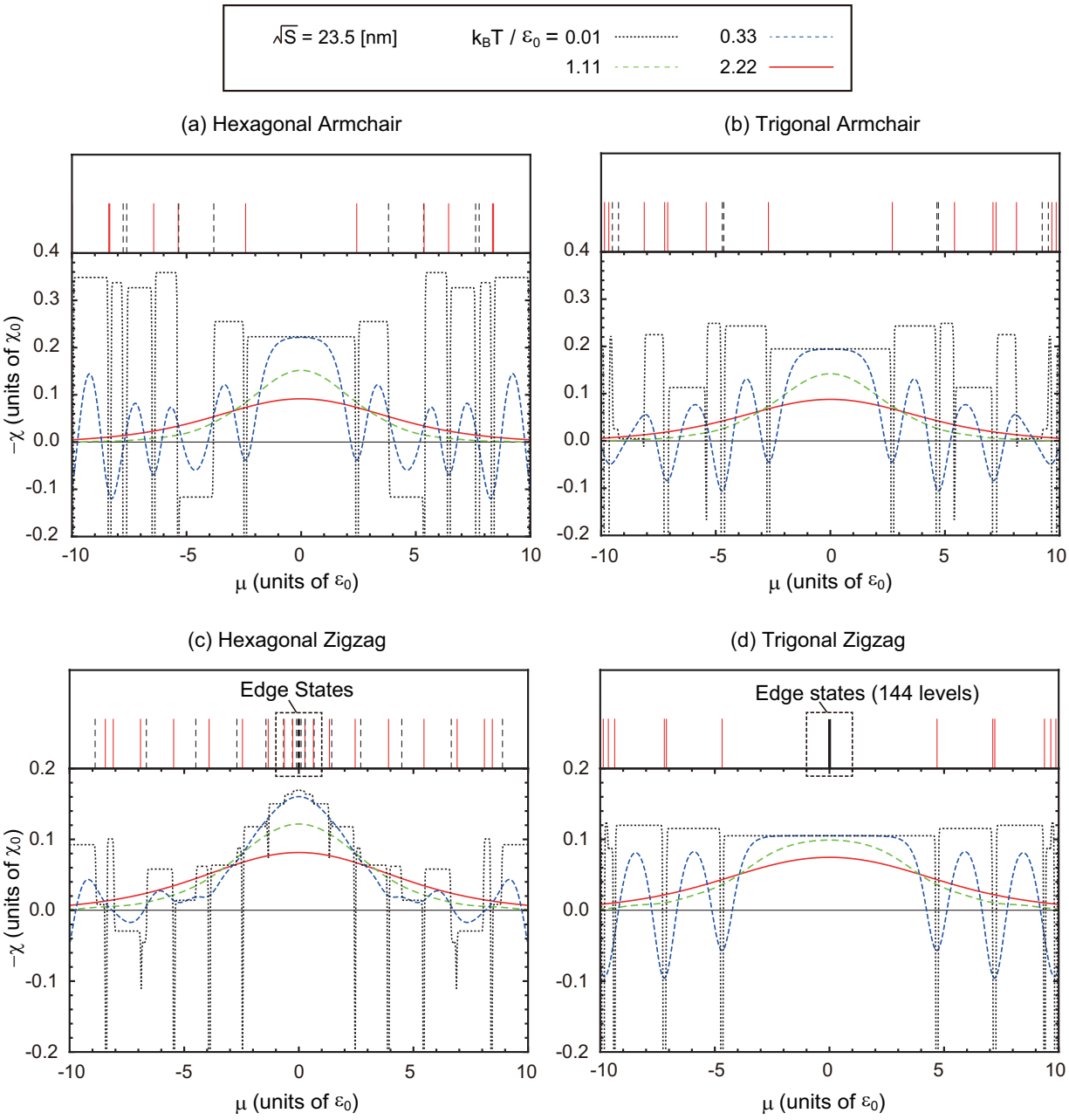

Figure 4.2: Energy level structure (upper panel) and magnetic susceptibility as a function of μ (lower) at several different temperatures, of (a) hexagonal armchair, (b) trigonal armchair, (c) hexagonal zigzag, and (d) trigonal zigzag graphene flakes with the size of $S \approx (23.5\text{nm})^2$. In the upper panel, dashed (black) lines represent non-degenerate levels, and solid (red) lines two-fold degenerate levels.

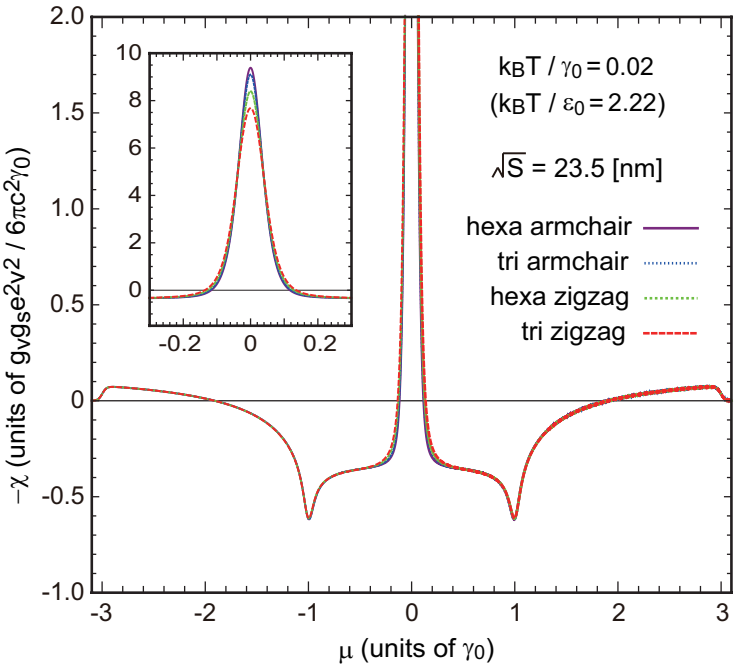

Figure 4.3: Extended plot of the susceptibility curve of $k_{\rm B}T/\varepsilon_0 = 2.22$ in Fig. 4.2, over the whole band region. The energy axis is now scaled by absolute unit γ_0, and the temperature amounts to $k_{\rm B}T/\gamma_0 = 0.02$ in this unit. Inset shows the detail of the central peak.

from the Dirac cone, with relative units ε_0 and χ_0 depending on the system size. In (b), we see that the curve converges to a single universal curve as the size increases, indicating that the physics there is well described by Dirac equation. The susceptibility agrees with the bulk limit $\chi_{\rm Dirac}$ in the high temperature region $k_{\rm B}T \gg \varepsilon_0$, whereas in $k_BT \lesssim \varepsilon_0$ it deviates from $\chi_{\rm Dirac}$ and reaches some finite maximum value, where the descrete level structure becomes significant.

The universal curve depends on the detail of the flake shape and the edge configuration. In Fig. 4.4(c), we plot $\chi(\mu = 0; T)$ for four different types of graphene flakes in a similar fashion to Fig. 4.4(b). The flake sizes are set to $S \approx (23.5\text{nm})^2$, which is sufficiently large to achieve the universal limit. In low temperatures, the susceptibility tends to be larger in armchair flake than in zigzag flake, and larger in hexagonal flake than trigonal flake. A similar edge dependence is found in graphene ribbons, where armchair ribbons generally exhibit larger diamagnetism than zigzag ribbons. In the high temperature region, on the other hand, all the curves approaches the bulk limit.

4.3 Comparison to spin magnetism

The orbital magentism always competes with the spin magnetism which has been neglected so far. When we include spin Zeeman splitting, a spin-less energy level at E_0 is accompanied by the Pauli paramagnetism

$$\chi_{\rm Pauli} = \frac{2}{S}\left(\frac{g}{2}\right)^2 \mu_{\rm B}^2 \delta(\mu - E_0), \tag{4.11}$$

where $g \sim 2$ is the g factor for a graphene electron, $\mu_{\rm B} = e\hbar/(2m_0c)$ is the Bohr magneton and m_0 is the bare electron mass. This is similar to the orbital contribution Eq. (4.8), while there $\mu_{\rm B}$ is replaced with the orbital magnetic moment m. The typical magnitude

of m is shown to be of the order of $\sqrt{S}ev/c$, which is the only magnetic-moment scale in the massless Dirac system. m is typically much greater than $\mu_{\rm B}$, suggesting that the Pauli paramagentic effect is generally much smaller than the orbital effect. At $S = (1\text{nm})^2$, for example, $\sqrt{S}ev/c$ is already as large as $20\mu_{\rm B}$. This in contrast to conventional electron systems where orbital magnetic moment and spin magnetic moment are both of the order of $\mu_{\rm B}$. [74]

In a zigzag graphene flake, a bunch of edge states degenerate at zero energy give exceptionally large Pauli paramagnetism. The contribution is written as

$$\chi_{\rm Pauli} = N_{\rm edge}\frac{2}{S}\left(\frac{g}{2}\right)^2\mu_{\rm B}^2\delta(\mu), \tag{4.12}$$

where $N_{\rm edge}(\sim\sqrt{S}/a)$ is the number of edge states. In the low-temperature regime such that $k_BT \ll \varepsilon_0$, this is dominant over the orbital effect near zero energy, since the orbital susceptibility does not diverge at edge states as already shown. In high-temperature regime $k_BT \gg \varepsilon_0$, the delta-function is thermally broadened and it should be compared to the bulk orbital susceptibility $\chi_{\rm Dirac}$, Eq. (2.38). The ratio between two opposite components approximates

$$\left|\frac{\chi_{\rm Pauli}}{\chi_{\rm Dirac}}\right| \sim \frac{3\pi}{g_{\rm v}g_{\rm s}}\left(\frac{\hbar}{m_0va}\right)^2\left(\frac{g}{2}\right)^2\frac{a}{\sqrt{S}} \sim 0.4\times\frac{a}{\sqrt{S}}, \tag{4.13}$$

so that the Pauli paramagnetism is negligible in a large flake with $\sqrt{S} \gg a$. This is corresponding to Eq. (3.27).

It should be noted that graphene flakes may have lattice vacancies and/or adatoms depending on the experimental condition, and the impurity levels at these defects contribute to additional Pauli paramagnetism. Moreover, we remark that there are several experimental studies that report ferromagnetic spin ordering in graphene-based materials. [65, 66, 67, 69] The origin of the spontaneous magnetism is still under debate, while it can be in principle caused by the atomic defects, grain boundaries, and highly-degenerate edge states. [28, 43, 44]

4.4 Diamagnetic current distribution

Fig. 4.5 shows the diamagnetic current distribution induced by the magnetic field in the four types of graphene flakes of the size $S \approx (23.5\text{nm})^2$ at several different temperatures. To visualize the global current circulation, we illustrate continuous flux lines obtained by smoothing the original discrete current J_{mn} on each bond, which is shown in the left insets. Specifically, we find the potential function Ψ which satisfies $\boldsymbol{J} = \boldsymbol{e}_z \times \nabla\Psi$, and obtain the equi-potential lines of Ψ. At zero temperature, the flux circulates entirely on the system reflecting the absence of the characteristic wave length in graphene, while it gradually becomes localized near the edge as temperature becomes higher. The current circulation of zigzag and armchair graphene flakes are globally similar, but the flux lines of armchair flakes exhibit some roughness while it is not observed in zigzag flakes. This actually corresponds to the atomic-scale current circulation in the Kekulé pattern seen in the original current map, [28] which is caused by the inter-valley (between K and K′) hybridization peculiar to the armchair edge.

Fig. 4.6 shows the detailed plots of the electric current as a function of position from the boundary to the center, for (a) the zigzag and (b) armchair flake. The position is labeled by the bond index defined in the inset, and A and B (B') correspond to the edge and the

center of triangle (hexagon), respectively, which are depicted in Fig. 4.6(c). The current distribution is more edge-localized when T becomes higher, and the typical depth of the edge current is characterized by

$$\lambda_{\rm edge} = \frac{\hbar v}{2\pi k_{\rm B} T}, \tag{4.14}$$

as is consistent with the result for graphene ribbons. The current distribution in the atomic scale crucially depends on the edge type even in the high temperature regime, but we can show that the integrated edge current approximates $c\chi_{\rm Dirac}B$ independently of the edge type, as long as the diamagnetic current is well localized near the edge. When comparing hexagonal and triangular flakes of the same edge type, we see that the curves are almost completely equivalent in $k_{\rm B}T/\varepsilon_0 \gtrsim 2$. This suggests that the current distribution in the high temperature regime does not depend on the global shape any more but is solely determined by the edge configuration.

4.5 Randomly stacked multilayer graphene

The diamagnetism can be made even greater by stacking graphenes in three dimensions. The recent experimental technique realizes a novel kind of graphene multilayer in which successive layers are stacked with random rotating angles. [75, 76, 77] There it is known that the interlayer coupling is significantly weakened and the Dirac cone is kept almost intact near zero energy as long as the rotating angle is not too small. [78, 79, 80, 81] The orbital susceptibility of such a system is expected to be much stronger than graphite in which the delta-function peak of $\chi(\varepsilon_{\rm F})$ is much broadened and shortened by the regular interlayer coupling. [82, 83]

Here we consider the orbital diamagnetism of a finite-sized piece of random-stacked graphene multilayers. In calculations, we self-consistently include the effect of the counter magnetic field induced by the diamagnetic current itself. This is essential because, as we will show in the following, the counter magnetic field of this system can be of the same order of the external magnetic field, and even nearly perfect screening is possible in low temperatures.

For simplicity, we completely neglect the interlayer coupling and regard the system as a set of independent single layer graphenes. We also assume that each layer has the identical shape with a characteristic length scale L, and that the system is large enough that the thermal broadening energy $k_{\rm B}T$ is much larger than $2\pi\hbar v/L$. According to the previous discussions, we then expect that the susceptibility of each layer is given by the bulk limit $\chi_{\rm Dirac}$ in Eq. (2.38), and also the depth of the edge current $\lambda_{\rm edge}$ of Eq. (3.24) can be neglected with respect to the system size L.

Let us consider a situation where a external field $B_{\rm ext}$ is applied perpendicularly to graphene plane of the random stacked multilayer. The total magnetic field B penetrating the system is

$$B = B_{\rm ext} + \Delta B, \tag{4.15}$$

where ΔB is the counter field caused by graphene electrons. The total field B induces the magnetism in each layer, $M = \chi_{\rm Dirac}BS$, with S being the area of the layer. This is related to the diamagnetic edge current I of each single layer by

$$I = \frac{cM}{S} = c\chi_{\rm Dirac}B. \tag{4.16}$$

Since the ring current I exists every interlayer distance d, it induces a counter-magnetic field inside the system as

$$\Delta B = \frac{4\pi}{c}\frac{I}{d}. \tag{4.17}$$

Solving the set of equations, we find that the dimensionless volume susceptibility becomes

$$\chi_{3\mathrm{D}} \equiv \frac{\Delta B}{B_{\mathrm{ext}}} = \frac{-1}{1 - d/(4\pi\chi_{\mathrm{Dirac}})}. \tag{4.18}$$

At the charge neutral point $\mu = 0$, in particular, we have

$$\chi_{3\mathrm{D}}(\mu = 0) = \frac{-1}{1 + k_{\mathrm{B}}T/\Delta}, \tag{4.19}$$

where Δ is a characteristic energy scale defined by

$$\Delta = \frac{g_v g_s}{6}\left(\frac{v}{c}\right)^2 \frac{e^2}{d} \approx 0.03\mathrm{meV}, \tag{4.20}$$

and d is assumed to be the interlayer spacing of graphite, 0.334 nm.

In decreasing the temperature, $\chi_{3\mathrm{D}}$ monotonically increases in the negative direction, and approaches -1, where the perfect magnetic field screening is achieved. This reflects the property of the single-layer susceptibility, Eq. (2.38), of which peak value at Dirac point diverges in $T \to 0$. In contrast, $\chi_{3\mathrm{D}}$ of the graphite is of the order of 10^{-4} and is not much enhanced in low temperatures, [84] because $\chi(\varepsilon_{\mathrm{F}})$ is already broadened by the interlayer coupling energy about 4000 K. [82, 83] A three-dimensional bulk material composed of random-stacked graphenes, if realized, would be the strongest diamagnetic material than any other known substances except for the superconductors.

4.6 Magnetic field alignment of graphene flakes

The diamagnetism of graphene can be possibly observed using the magnetic-field alignment of graphene nanoflakes dissolved in a solvent, similarly to the experiments for the carbon nanotube.[85] In a magnetic field, the graphene flakes tends to be oriented parallel to the field direction, because the field component penetrating the graphene plane raises the total energy due to the diamagnetism. If we assume that the graphene flakes are planer and rigid, the condition to achieve the alignment is roughly estimated as

$$\frac{1}{2}\chi B^2 S \gtrsim k_{\mathrm{B}}T. \tag{4.21}$$

For the graphene flakes $S = (23.5\mathrm{nm})^2$ at $T = 300\mathrm{K}$, for example, the required field becomes $B \gtrsim 9\mathrm{T}$.

We calculate the angle distribution of graphene flakes in various magnetic fields using the Maxwell-Boltzmann statistics. In the thermal equilibrium, the probability that the normal of the graphene plane is inclined from the magnetic field by θ to $\theta + d\theta$ is written as $P(\cos\theta)d(\cos\theta)$, where

$$P(\cos\theta) = \frac{\exp[-\beta U(\cos\theta)]}{\int_{-1}^{1}\exp[-\beta U(\cos\theta)]\mathrm{d}(\cos\theta)}, \tag{4.22}$$

with $U(\cos\theta) = -\chi B^2 S \cos^2\theta/2$ and $\beta = 1/(k_{\mathrm{B}}T)$. Fig. 4.7 plots the distribution function $P(\cos\theta)$ for the hexagonal armchair flakes with several sizes at $T = 300$K, calculated using χ in Fig. 4.4(a). We see that the alignment occurs more strongly in larger flakes, because the magnetization of a single flake, χSB, is greater for larger S. Note that it is not only due to a linear factor S, but also because χ increases in larger S as shown in Fig. 4.4(a).

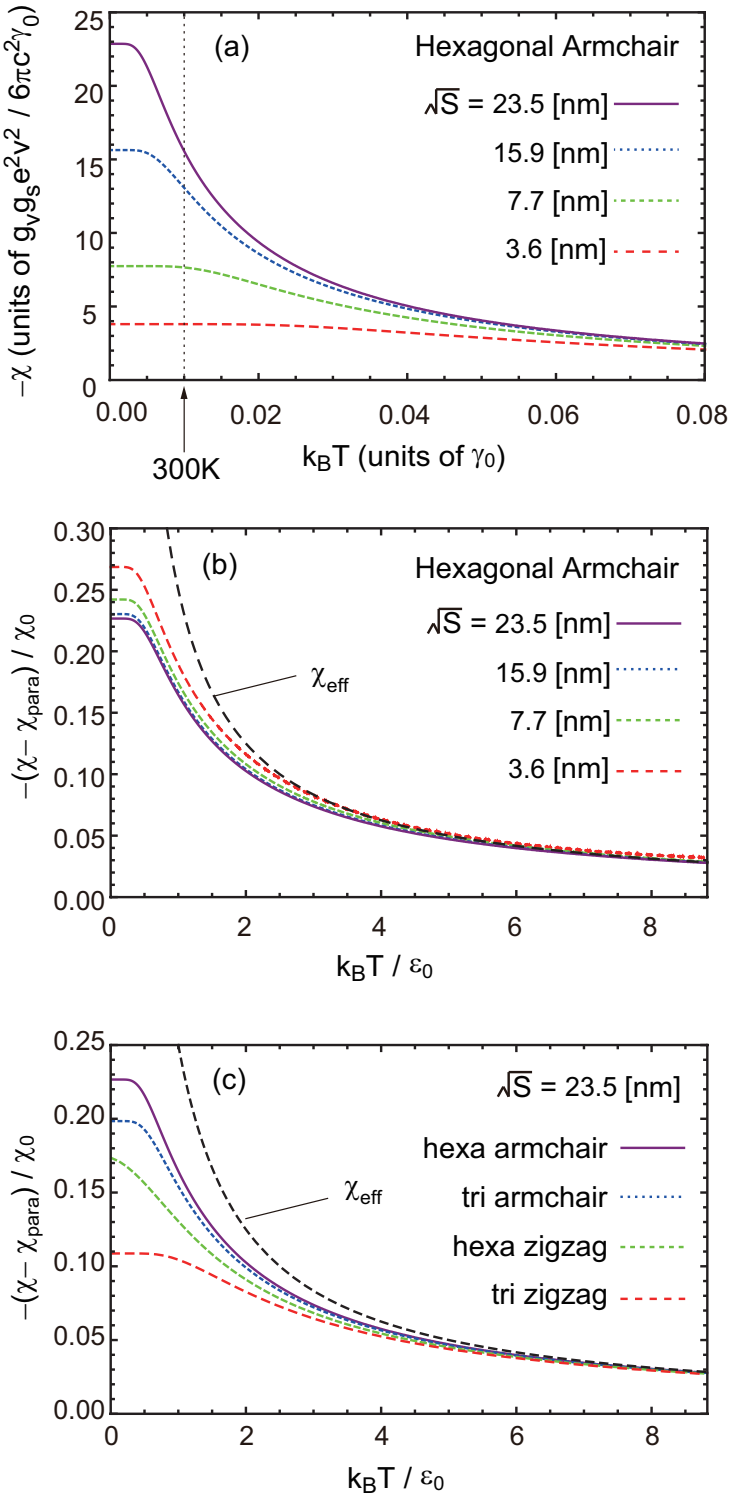

Figure 4.4: (a) $\chi(\mu = 0; T)$ of hexagonal armchair flakes with several different sizes, plotted in the absolute units γ_0 and $g_v g_s e^2 v^2/(6\pi c^2 \gamma_0)$. (b) $\chi(\mu = 0; T) - \chi_{\rm para}$ of the same systems, plotted in the relative units ε_0 and $g_v g_s e^2 v^2/(6\pi c^2 \varepsilon_0)$. (c) Plot similar to (b) for four different types of graphene flakes with the size $S \approx (23.5\text{nm})^2$.

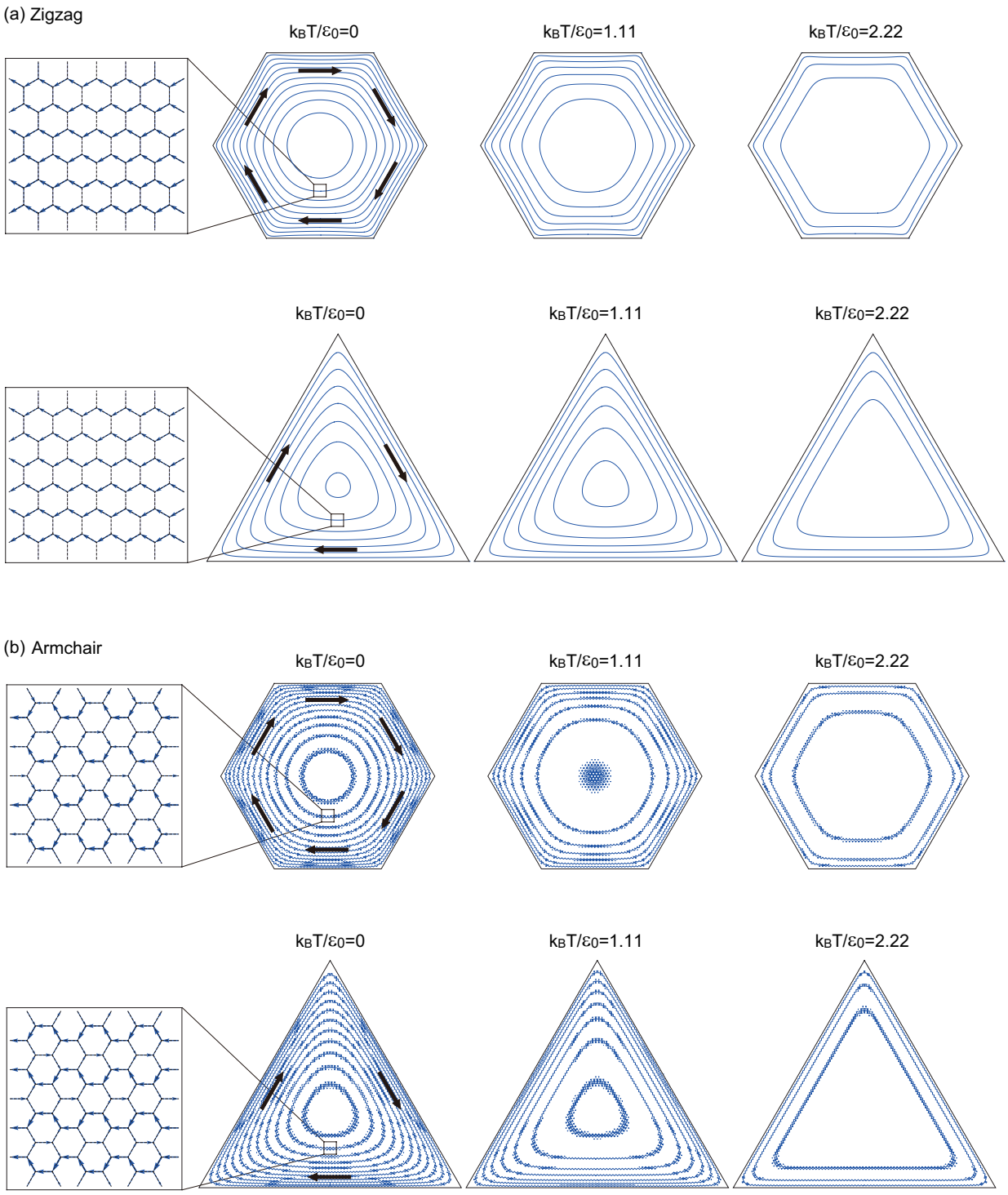

Figure 4.5: Diamagnetic current distribution in the four types of graphene flakes of the size $S \approx (23.5\text{nm})^2$ at several different temperatures. Continuous flux lines are obtained by smoothing the original discrete current on each bond, which is shown in left insets.

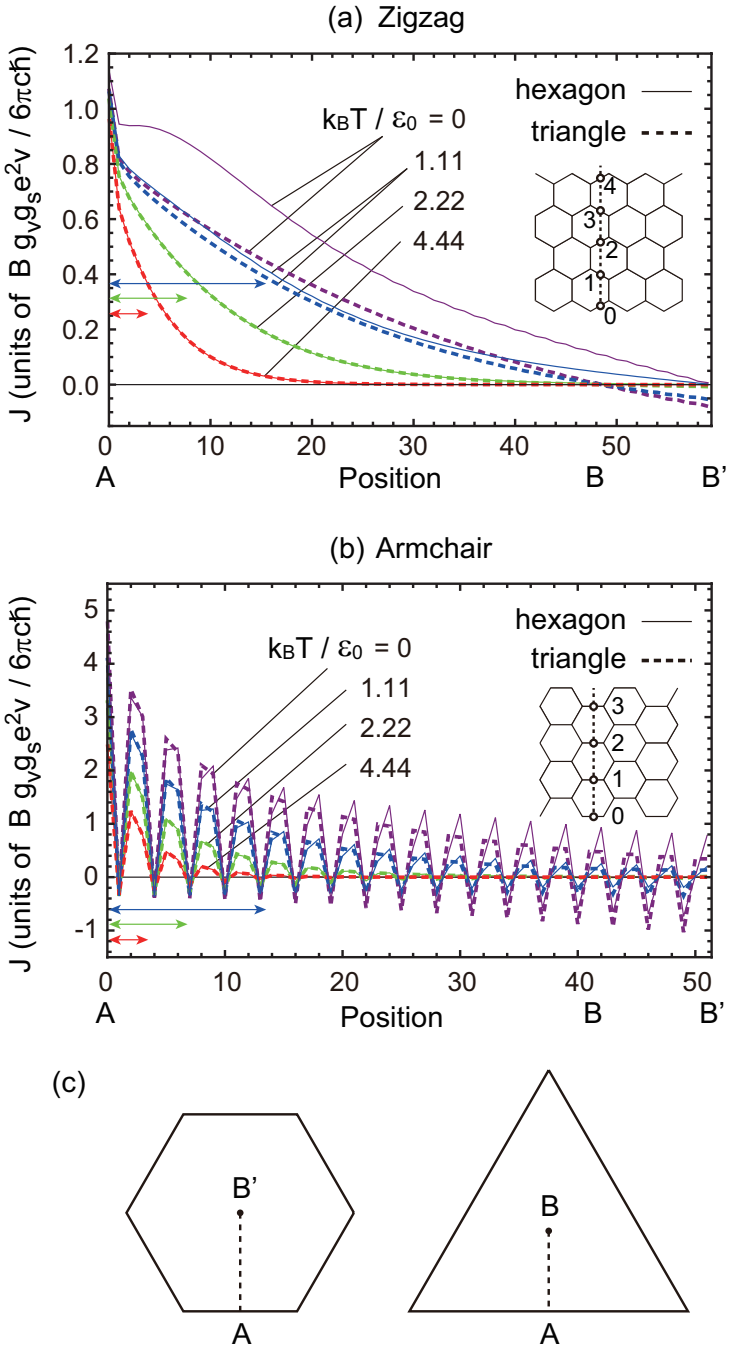

Figure 4.6: Electric current as a function of position from the boundary to the center, for (a) the zigzag and (b) armchair flake of $S \approx (23.5\text{nm})^2$. The position is labeled by the bond index defined in the inset, and A and B (B') represent the border and the center of triangle (hexagon), respectively, which are specified in (c). Horizontal arrows indicate λ_{edge} for $k_BT/\varepsilon_0 = 1.11, 2.22$ and 4.44.

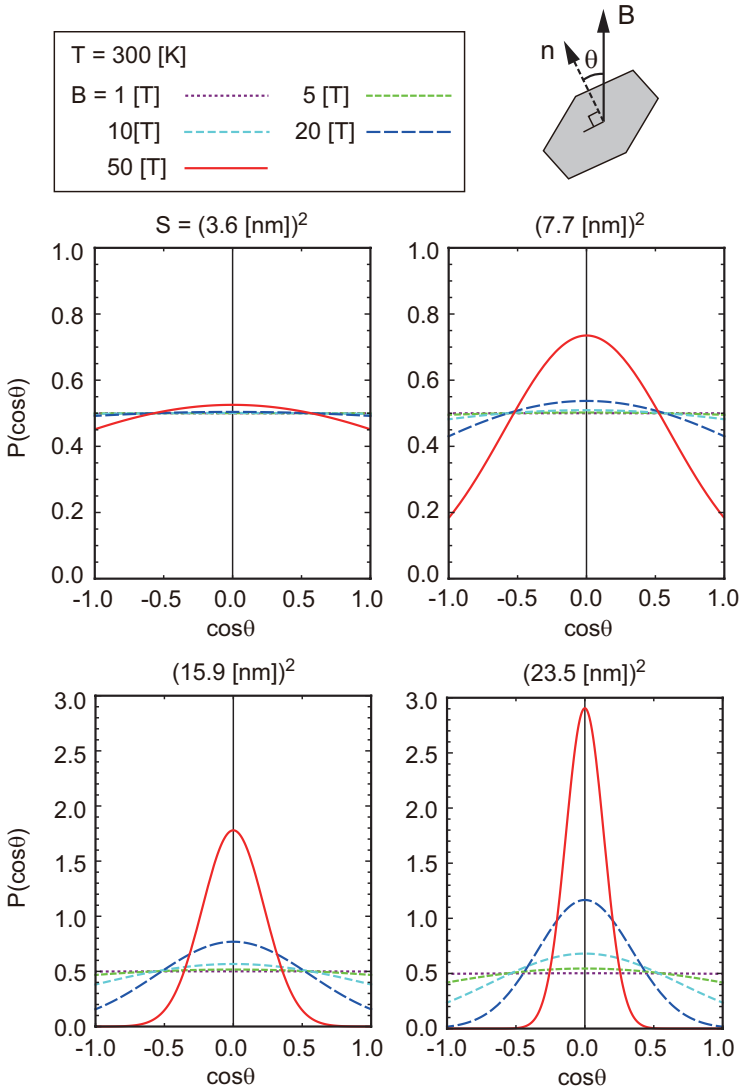

Figure 4.7: Angle distribution in magnetic fields, calculated for hexagonal armchair flakes with several sizes at $T = 300$K.

Chapter 5

Summary and Conclusion

We have studied the orbital magnetism of the graphene ribbons and the graphene flakes with various shapes and edge configurations, to figure out the effect of quantum confinement on the singular diamagentism in the bulk graphene. We found that the behavior is significantly different depending on the relative magnitude of the thermal broadening energy $k_{\mathrm{B}}T$ to the characteristic level spacing ε_0 due to the quantum comfinement. In the low-temperature regime where $k_{\mathrm{B}}T \ll \varepsilon_0$, the susceptibility as a function of Fermi energy rapidly changes between diamagnetism and paramagnetism in accordance with the level structure which depends on the specific atomic structure of the system. The qualitative feature does not strongly depend on the edge configuration or global shape, but the susceptibility around the zero Fermi energy tends to be larger in armchair edges than in zigzag edges, and larger in hexagonal flakes than trigonal flakes. In the high-temperature regime $k_{\mathrm{B}}T \ll \varepsilon_0$, on the other hand, the oscillatory structures due to the finite-size effect are all gone, and the susceptibility approaches the bulk limit independently of the shape and the edge configuration of the graphene nanostructures. We also see a carbon nanotube, another form of quasi-one-dimensional carbon, exhibits a similar oscillation in $\chi(\varepsilon_F)$, but the overall magnitude is reduced by a factor 2 compared to the corresponding ribbon having the same width.

The diamagnetic current circulates entirely over the graphene nanostructures in the low-temperature regime, reflecting the absence of characteristic length scale in the massless Dirac system. As temperature increases, the current gradually becomes to circulate only near the edge, with the characteric depth of $\lambda_{\mathrm{edge}} = \hbar v/2\pi k_{\mathrm{B}}T$. The local current distribution along the cross section prependicular to the boundary is independent of the global shape, while its detalied property in the atomic scale is significantly different between armchair and zigzag edges. The result of the current distribution is applied to estimate the three-dimensional bulk susceptibility of random-stacked multilayer graphene. There we showed that the external magnetic field is significantly screened inside the sample, realzing the analog of Meissner effect in superconductors.

We propose that the diamagnetism of graphene can be possibly observed using the magnetic-field alignment of graphene flakes. We estimated the angle distribution for given magnetic field at the room temperature, and found that a strong alignment could be realized in the feasible magnetic field range for flakes of $S \gtrsim (10\mathrm{nm})^2$.

Acknowledgments

I would like to express my sincerest gratitude to Associate Professor Mikito Koshino for his continual guidance and encouragement throughout the course of the present work and his critical reading of the manuscript. I appreciate discussions with all the members of the condensed matter physics theory group.

Appendix A

Landau diamagnetism

In this section, we review the orbital diamagnetism of conventional two-dimensional electron gas (2DEG), which is well known as the Landau diamagnetism. Here we consider the Hamiltonian in two dimensions,

$$\mathcal{H} = \frac{\boldsymbol{\pi}^2}{2m^*}, \tag{A.1}$$

where $\boldsymbol{\pi} = \boldsymbol{p} + (e/c)\boldsymbol{A}$, $\boldsymbol{p} = (p_x, p_y)$, and m^* is an effective-mass. Landau levels, or the energy levels in the presence of the magnetic field perpendicular to the plane are derived as

$$\varepsilon_n = \hbar\omega_{\rm c}\left(n + \frac{1}{2}\right), \quad (n = 0, 1, 2, \cdots), \tag{A.2}$$

where $\omega_{\rm c} = eB/(m^*c)$ is the cyclotron frequency. Each Landau level has degeneracy $g = 1/(2\pi\ell_{\rm B})$ per area, with magnetic length $\ell_{\rm B}$

$$\ell_{\rm B} = \sqrt{\frac{c\hbar}{eB}}. \tag{A.3}$$

The thermodynamic potential Ω is given by

$$\Omega = -k_{\rm B}T g_{\rm v} g_{\rm s} g \sum_{n=0}^{\infty} \ln\{1 + \exp[(\mu - \varepsilon_n)/k_{\rm B}T]\}, \tag{A.4}$$

where $g_{\rm v}$ and $g_{\rm s}$ are the valley and spin degeneracy, respectively. Using the Euler-Maclaurin sum formula,

$$h\sum_{n=0}^{\infty} F\left[h\left(n + \frac{1}{2}\right)\right] = \int_0^{\infty} F(x){\rm d}x + \frac{h^2}{24}[F'(0) - F'(\infty)] + \cdots, \tag{A.5}$$

where h is a small positive number, and $F(x)$ is a smooth function, Ω is calculated as

$$\begin{aligned}
\Omega &= -k_{\rm B}T g_{\rm v} g_{\rm s} g \sum_{n=0}^{\infty} \ln\{1 + \exp[\{\mu - \hbar\omega_{\rm B}(n + 1/2)\}/k_{\rm B}T]\}, \\
&= -k_{\rm B}T g_{\rm v} g_{\rm s} g \frac{1}{\hbar\omega_{\rm c}}\Bigg[\int_0^{\infty} \ln\{1 + \exp[(\mu - \varepsilon)/k_{\rm B}T]\}{\rm d}\varepsilon \\
&\qquad - \frac{\hbar\omega_{\rm c}}{24}\frac{\exp(\mu/k_{\rm B}T)/k_{\rm B}T}{1 + \exp(\mu/k_{\rm B}T)} + \cdots\Bigg].
\end{aligned} \tag{A.6}$$

Up to the order of B^2, $\Delta\Omega$ is written as

$$\begin{aligned}\Delta\Omega &\approx g_{\mathrm{v}} g_{\mathrm{s}} \frac{m^*}{2\pi\hbar^2} \frac{(\hbar\omega_{\mathrm{c}})^2}{24} \frac{1}{\exp(-\mu/k_{\mathrm{B}}T)+1} \\ &= \frac{1}{6} g_{\mathrm{v}} g_{\mathrm{s}} \mu_{\mathrm{B}}^2 D_{2\mathrm{d}} B^2 \frac{1}{\exp(-\mu/k_{\mathrm{B}}T)+1} \end{aligned} \tag{A.7}$$

where $\mu_{\mathrm{B}} = e\hbar/(2m^*c)$, and $D_{2\mathrm{d}} = m^*/(2\pi\hbar^2)$ is a density of states for two-dimensional electron gas per area. Using Eq. (2.30) and (A.7), the susceptibility is derived as

$$\chi(\mu;T) = -\frac{1}{3} g_{\mathrm{v}} g_{\mathrm{s}} \mu_{\mathrm{B}}^2 D_{2\mathrm{d}} \frac{1}{\exp(-\mu/k_{\mathrm{B}}T)+1}. \tag{A.8}$$

In the limit of $T \to 0$, it beomces

$$\chi(\varepsilon_F) = -\frac{1}{3} g_{\mathrm{v}} g_{\mathrm{s}} \mu_{\mathrm{B}}^2 D_{2\mathrm{d}} \theta(\varepsilon_F) \tag{A.9}$$

Appendix B

Orbial magnetism of 2DEG ribbon

We consider the orbital magenetism of 2DEG confined in a ribbon. We assume that the system has translational symmetry to y direction, and is confined in x direction from 0 to L_x. The eigenstates and the subband of the system is derived as

$$\begin{aligned}
\psi_{nk_y}(x,y) &= \sqrt{\frac{2}{L_x L_y}} e^{ik_y y} \sin k_n x, \\
\varepsilon_{nk_y} &= \frac{\hbar^2 k_y^2}{2m^*} + \frac{\hbar^2 \pi^2}{2m^* L_x^2} n^2, \\
k_n &= \frac{\pi}{L_x} n, \quad (n = 1, 2, \cdots).
\end{aligned} \tag{B.1}$$

For the normalization of the wave function, we assumed the periodic boundary condition in the y direction with a large enough period L_y.

In the presence of the magnetic field B perpendicular to the 2D plane, Hamiltonian is given by

$$\begin{aligned}
\mathcal{H} &= \mathcal{H}_0 + \delta\mathcal{H}, \\
\delta\mathcal{H} &= \frac{e}{c} \boldsymbol{v} \cdot \boldsymbol{A} + \frac{e^2 \boldsymbol{A}^2}{2m^* c^2},
\end{aligned} \tag{B.2}$$

where $\mathcal{H}_0$ is the unperturbed Hamiltonian, and $\boldsymbol{v} = \partial\mathcal{H}_0/\partial\boldsymbol{p}$ is velocity operator. We treat $\delta\mathcal{H}$ as a perturbation, and calculate electric current induced by magnetic field and orbital magnetic susceptibility numerically in the same way as in the graphene ribbons. The typical energy scale for the subband structure and the characteristic unit of the susceptibility are taken as

$$\varepsilon_0 = \frac{\hbar^2 \pi^2}{2m^* L_x^2}, \tag{B.3}$$

$$\chi_0 = \frac{1}{3} g_{\mathrm{v}} g_{\mathrm{s}} \mu_{\mathrm{B}}^2 D_{\mathrm{2d}}, \tag{B.4}$$

respectively.

The upper panel and lower panel of Fig. B.1 show the subband structure and the magnetic susceptibility as a function of μ, respectively. At zero temperature, the susceptibility oscillates as a function of ε_{F} in accordance with the subband structure, while as temperature increases, the oscillation gradually disappears and approaches the bulk susceptibility Eq. (A.8). The temperature required to reach the bulk limit is larger in higher μ, because the subband interval, which is proportional to subband label n, is wider in higher energy.

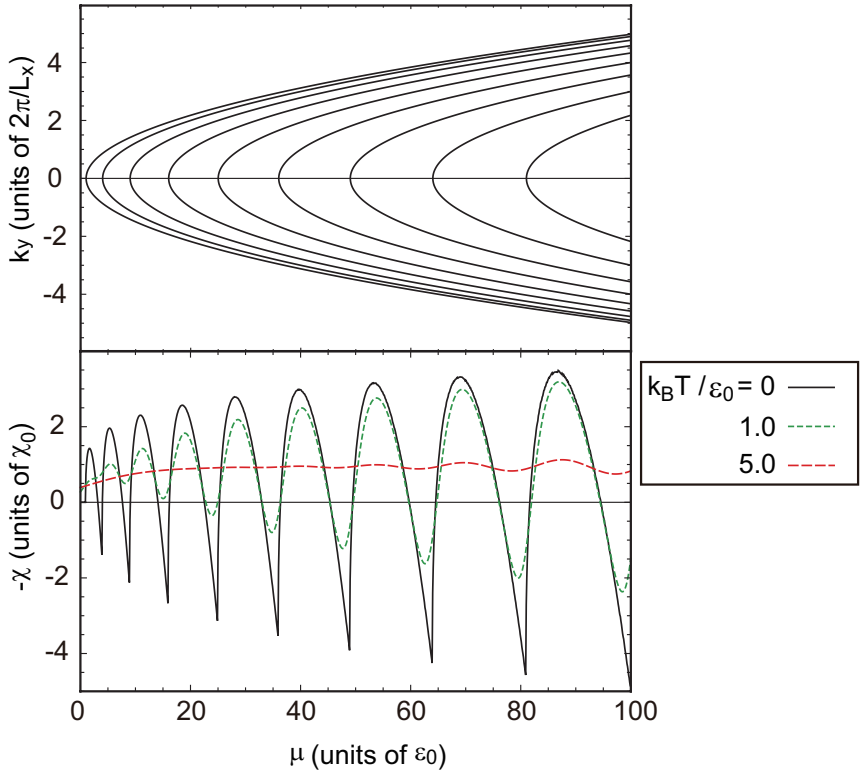

Figure B.1: Magnetic susceptibility as a function of Fermi energy.

Fig. B.2 shows the diamagnetic current density as a function of position x. We see that at zero temperature, the current density oscillates as a function of x in the period of the order of the Fermi wavelength λ_{F}, while as the temperature increase and the thermal energy $k_{\mathrm{B}}T$ exceeds the subband interval, the current is distributed near the edge with the depth of the order of λ_{F}.

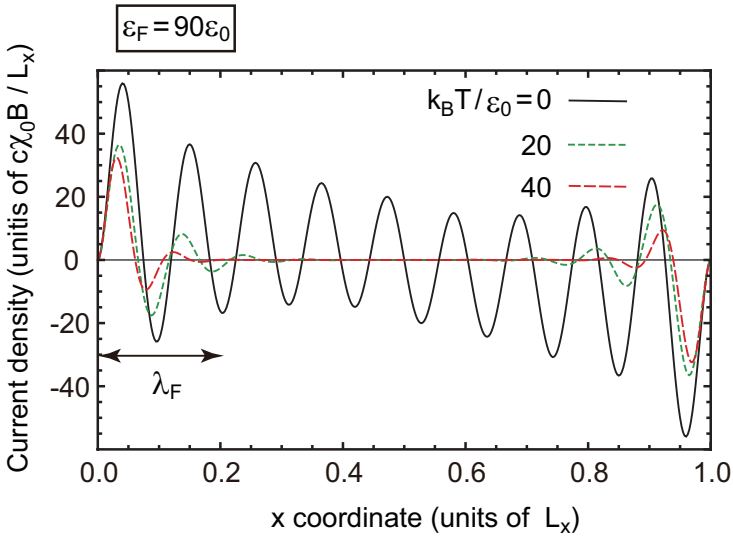

Figure B.2: Diamagnetic current density induced by magnetic field.

Bibliography

[1] P.R. Wallace, Phys. Rev. **71**, 622 (1947).

[2] J. C. Slonczewski and P. R. Weiss, Phys. Rev. **109**, 272 (1958).

[3] J. W. McClure, Phys. Rev. **104**, 666 (1956).

[4] M. S. Dresselhaus, G. Dresselhaus, and P. C. Eklund, *Science of Fullerenes and Carbon Nanotubes* (Academic, New York, 1996).

[5] K. S. Novoselov, A. K. Geim, S. V. Morozov, D. Jiang, Y. Zhang, S. V. Dubonos, I. V. Grigorieva, and A. A. Firsov, Science **306**, 666 (2004).

[6] A. H. Castro Neto, F. Guinea, N. M. Peres, K. S. Novoselov, and A. K. Geim, Rev. Mod. Phys. **81**, 109 (2009).

[7] D. P. DiVincenzo and E. J. Mele, Phys. Rev. B **29**, 1685 (1984).

[8] G. W. Semenoff, Phys. Rev. Lett. **53**, 2449 (1984).

[9] T. Ando, J. Phys. Soc. Jpn. **74**, 777 (2005).

[10] N. H. Shon and T. Ando, J. Phys. Soc. Jpn. **67**, 2421 (1998).

[11] T. Ando, Y. Zheng, and H. Suzuura, J. Phys. Soc. Jpn. **71**, 1318 (2002).

[12] Y. Zheng and T. Ando, Phys. Rev. B **65**, 245420 (2002).

[13] K. S. Novoselov, A. K. Geim, S. V. Morozov, D. Jiang, M. I. Katsnelson, I. V. Grigorieva, S. V. Dubonos, and A. A. Firsov, Nature **438**, 197 (2005).

[14] Y. Zhang, Y.-W. Tan, H. L. Stormer, and P. Kim, Nature **438**, 201 (2005).

[15] A. B. Kuzmenko, E. van Heumen, F. Carbone, and D. van der Marel, Phys. Rev. Lett. **100**, 117401 (2008).

[16] R. R. Nair, P. Blake, A. N. Grigorenko, K. S. Novoselov, T. J. Booth, T. Stauber, N. M. R. Peres, and A. K. Geim, Science **320**, 1308 (2008).

[17] M. Y. Han, B. Özyilmaz, Y. Zhang, and P. Kim, Phys. Rev. Lett. **98**, 206805 (2007).

[18] Z. Chen, Y.-M. Lin, M. J. Rooks, and P. Avouris, Physica E **40**, 228 (2007).

[19] X. Li, X. Wang, L. Zhang, S. Lee, and H. Dai, Science **319**, 1229 (2008).

[20] D. V. Kosynkin, A. L. Higginbotham, A. Sinitskii, J. R. Lomeda, A. Dimiev, B. K. Price, and J. M. Tour, Nature **458**, 872 (2009).

[21] L. Jiao, L. Zhang, X. Wang, G. Diankov, and H. Dai, Nature **458**, 877 (2009).

[22] S. K. Hamalainen, X. Sun, M. P. Boneschanscher, A. Uppstu, M. Ijas, A. Harju, D. Vanmaekelbergh, and P. Liljeroth Phys. Rev. Lett. **107**, 236803 (2011).

[23] D. Subramaniam, F. Libisch, Y. Li, C. Pauly, V. Geringer, R. Reiter, T. Mashoff, M. Liebmann, J. Burgdorfer, C. Busse, T. Michely, R. Mazzarello, M. Pratzer, and M. Morgenstern Phys. Rev. Lett. **108**, 046801 (2012).

[24] D. Geng, B. Wu, Y. Guo, L. Huang, Y. Xue, J. Chen, G. Yu, L. Jiang, W. Hu, and Y. Liu, Proc. Natl. Acad. Sci. USA **109**, 7992 (2012).

[25] M. Fujita, K. Wakabayashi, K. Nakada, and K. Kusakabe, J. Phys. Soc. Jpn. **65**, 1920 (1996).

[26] Y. Kobayashi, K. Fukui, T. Enoki, K. Kusakabe, and Y. Kaburagi, Phys. Rev. B **71**, 193406 (2005).

[27] K. Nakada, M. Fujita, G. Dresselhaus, and M. S. Dresselhaus, Phys. Rev. B **54**, 17954 (1996).

[28] K. Wakabayashi, M. Fujita, H. Ajiki, and M. Sigrist, Phys. Rev. B**59**, 8271 (1999).

[29] M. Ezawa, Phys. Rev. B **73**, 045432 (2006).

[30] L. Brey, and H. Fertig, Phys. Rev. B **73**, 195408 (2006).

[31] L. Brey, and H. Fertig, Phys. Rev. B **73**, 235411 (2006).

[32] Y-W. Son, M. L. Cohen, S. G. Louie, Phys. Rev. Lett. **97**, 216803 (2006).

[33] Y-W. Son, M. L. Cohen, S. G. Louie, Nature **444**, 347 (2006).

[34] K. Wakabayashi, Y. Takane, and M. Sigrist, Phys. Rev. Lett. **99**, 036601 (2007).

[35] M. Ezawa, Phys. Rev. B **76**, 245215 (2007).

[36] M. Ezawa, Phys. Rev. B **81**, 201402 (2010).

[37] M. Zarenia, A. Chaves, G. A. Farias, and F. M. Peeters, Phys. Rev. B **84**, 245403 (2011).

[38] P. Potasz, A. D. Guclu, and P. Hawrylak, Phys. Rev. B **81**, 033403 (2010).

[39] D. A. Bahamon, A. L. C. Pereira, and P. A. Schulz, Phys. Rev. B **79**, 125414 (2009).

[40] J. Akola, H. P. Heiskanen, and M. Manninen Phys. Rev. B **77**, 193410 (2008).

[41] Z. Z. Zhang and Kai Chang, Phys. Rev. B **77**, 235411 (2008).

[42] D. P. Kosimov, A. A. Dzhurakhalov, and F. M. Peeters, Phys. Rev. B **81**, 195414 (2010).

[43] J. Fernandez-Rossier and J. J. Palacios, Phys. Rev. Lett. **99**, 177204 (2007).

[44] W. L. Wand, S. Meng, and E. Kaxiras, Nano Lett. **8**, 241 (2008).

[45] J. W. McClure, Phys. Rev. **119**, 606 (1960).

[46] M. P. Sharma, L. G. Johnson, and J. W. McClure, Phys. Rev. B **9**, 2467 (1974).

[47] H. Fukuyama and R. Kubo, J. Phys. Soc. Jpn. **27**, 604 (1969). Interband effect on magnetic susceptibility. I. A simple two-band model

[48] H. Fukuyama and R. Kubo, J. Phys. Soc. Jpn. **28**, 570 (1970). Interband effect on magnetic susceptibility. II. Diamagnetism of bismuth

[49] S. A. Safran and F. J. DiSalvo, Phys. Rev. B **20**, 4889 (1979).

[50] T. Ando, Physica E **40**, 213 (2007).

[51] S. G. Sharapov, V. P. Gusynin, and H. Beck, Phys. Rev. B **69**, 075104 (2004).

[52] H. Fukuyama, J. Phys. Soc. Jpn. **76**, 043711 (2007).

[53] M. Nakamura, Phys. Rev. B **76**, 113301 (2007).

[54] M. Koshino and T. Ando, Phys. Rev. B **75**, 235333 (2007).

[55] A. Ghosal, P. Goswami, and S. Chakravarty, Phys. Rev. B **75**, 115123 (2007).

[56] M. Koshino and T. Ando, Phys. Rev. B **81**, 195431 (2010).

[57] M. Koshino, Y. Arimura, and T. Ando, Phys. Rev. Lett. **102**, 177203 (2009).

[58] J. Blinowski and C. Rigaux, J. Phys. (Paris) **45**, 545 (1984).

[59] R. Saito and H. Kamimura, Phys. Rev. B **33**, 7218 (1986).

[60] H. Ajiki and T. Ando, J. Phys. Soc. Jpn. **62**, 2470 (1993); J. Phys. Soc. Jpn. **63**, 4267 (1994) (Erratum).

[61] H. Ajiki and T. Ando, J. Phys. Soc. Jpn. **64**, 4382 (1995).

[62] M. Yamamoto, M. Koshino, and T. Ando, J. Phys. Soc. Jpn. **77**, 084705 (2008).

[63] J. Liu, Z. Ma, A. R. Wright, and and Chao Zhang, J. Appl. Phys. **103**, 103711 (2008).

[64] K. S. Krishnan and N. Ganguli, Nature 139, 155 (1937); Z. Krist. A100, 530 (1939).

[65] P. Esquinazi, A. Setzer, R. Hohne, and C. Semmelhack, Y. Kopelevich, D. Spemann and T. Butz, B. Kohlstrunk and M. Losche, Phys. Rev. B **66**, 024429 (2002).

[66] P. Esquinazi, D. Spemann, R. Hohne, A. Setzer, K.-H. Han, and T. Butz, Phys. Rev. Lett. **91**, 227201 (2003).

[67] T. Enoki and K. Takai, Solid State Commun. **149**, 1144 (2009).

[68] M. Sepioni, R. R. Nair, S. Rablen, J. Narayanan, F. Tuna, R. Winpenny, A. K. Geim, and I.V. Grigorieva, Phys. Rev. Lett. **105**, 207205 (2010).

[69] Y. Wang, Y. Huang, Y. Song, X. Zhang, Y. Ma, J. Liang, and Y. Chen, Nano Lett. **9**, 220 (2009).

[70] M. S. Dresselhaus, and G. Dresselhaus, Adv. Phys. **30**, 139 (1981).

[71] L. M. Zhang, Z. Q. Li, D. N. Basov, and M. M. Fogler, Phys. Rev. B **78**, 235408 (2008).

[72] S. Iijima, Nature (London) **354**, 56 (1991).

[73] S. Iijima, T. Ichihashi and Y. Ando, Nature **356**, 776 (1992).

[74] R. Kubo and Y. Obata, J. Phys. Soc. Jpn. **11**, 547 (1956).

[75] C. Berger, Z. Song, X. Li, X. Wu, N. Brown, C. Naud, D. Mayou, T. Li, J. Hass, A. N. Marchenkov, E. H. Conrad, P. N. First, and W. A. de Heer, Science **312**, 1191 (2006).

[76] J. Hass, R. Feng, J. E. Millan-Otoya, X. Li, M. Sprinkle, P. N. First, W. A. de Heer, E. H. Conrad, and C. Berger, Phys. Rev. B 75, 214109 (2007).

[77] G. Li, A. Luican and E. Y. Andrei, Phys. Rev. Lett. **102**, 176804 (2009).

[78] J. M. B. Lopes dos Santos, N. M. R. Peres, A.H. Castro Neto, Phys. Rev. Lett. 99, 256802 (2007).

[79] S. Latil, V. Meunier, and L. Henrard, Phys. Rev. B 76, 201402(R) (2007).

[80] S. Shallcross, S. Sharma and O.A. Pankratov, Phys. Rev. Lett. **101**, 056803 (2008).

[81] E. J. Mele, Phys. Rev. B **81**, 161405 (2010).

[82] S. A. Safran, Phys. Rev. B **30**, 421 (1984).

[83] M. Koshino and T. Ando, Phys. Rev. B **76**, 085425 (2007).

[84] K. S, Krishnan and N. Ganguli, Nature **139**, 155 (1937).

[85] S. Zaric, G. N. Ostojic, J. Kono, J. Shaver, V. C. Moore, M. S. Strano, R. H. Hauge, R. E. Smalley, X. Wei, Science **304**, 1129 (2004).

Publication list

1. Y. Ominato and M. Koshino, Phys. Rev. B **85**, 165454 (2012).
"Orbital magnetic susceptibility of finite-sized graphene"

2. Y. Ominato and M. Koshino, arXiv:1301.5440
"Orbital magnetism of graphene flakes"